



# TESS Giants Transiting Giants. II. The Hottest Jupiters Orbiting Evolved Stars

Samuel K. Grunblatt<sup>1,2,34</sup>, Nicholas Saunders<sup>3,35</sup>, Meng Sun<sup>4</sup>, Ashley Chontos<sup>3,35</sup>, Melinda Soares-Furtado<sup>4,36</sup>, Nora Eisner<sup>5</sup>, Filipe Pereira<sup>6,7</sup>, Thaddeus Komacek<sup>8,9,37</sup>, Daniel Huber<sup>3</sup>, Karen Collins<sup>10</sup>, Gavin Wang<sup>11</sup>, Chris Stockdale<sup>12</sup>, Samuel N. Quinn<sup>10</sup>, Rene Tronsgaard<sup>13</sup>, George Zhou<sup>10,14</sup>, Grzegorz Nowak<sup>15,16</sup>, Hans J. Deeg<sup>15,16</sup>, David R. Ciardi<sup>17</sup>, Andrew Boyle<sup>17</sup>, Malena Rice<sup>18,35</sup>, Fei Dai<sup>19</sup>, Sarah Blunt<sup>20</sup>, Judah Van Zandt<sup>21</sup>, Corey Beard<sup>22</sup>, Joseph M. Akana Murphy<sup>23,35</sup>, Paul A. Dalba<sup>23,24,38</sup>, Jack Lubin<sup>22</sup>, Alex Polanski<sup>25</sup>, Casey Lynn Brinkman<sup>3,35</sup>, Andrew W. Howard<sup>20</sup>, Lars A. Buchhave<sup>13</sup>, Ruth Angus<sup>1,2,26</sup>, George R. Ricker<sup>27</sup>, Jon M. Jenkins<sup>28</sup>, Bill Wohler<sup>28,29</sup>, Robert F. Goeke<sup>27</sup>, Alan M. Levine<sup>27</sup>, Knicole D. Colon<sup>30</sup>, Chelsea X. Huang<sup>14,27</sup>, Michelle Kunimoto<sup>27</sup>, Avi Shporer<sup>27</sup>, David W. Latham<sup>10</sup>, Sara Seager<sup>27,31,32</sup>, Roland K. Vanderspek<sup>27</sup>, and Joshua N. Winn<sup>33</sup>

<sup>1</sup> American Museum of Natural History, 200 Central Park West, Manhattan, NY 10024, USA

<sup>2</sup> Center for Computational Astrophysics, Flatiron Institute, 162 5th Avenue, Manhattan, NY 10010, USA

<sup>3</sup> Institute for Astronomy, University of Hawai'i at Mānoa, 2680 Woodlawn Drive, Honolulu, HI 96822, USA

<sup>4</sup> Department of Astronomy, University of Wisconsin Madison, Madison, WI 53726, USA

<sup>5</sup> Department of Physics, University of Oxford, Keble Road, Oxford OX1 3RH, UK

<sup>6</sup> Instituto de Astrofísica e Ciências do Espaço, Universidade do Porto, Rua das Estrelas, 4150-762 Porto, Portugal

<sup>7</sup> Departamento de Física e Astronomia, Faculdade de Ciências da Universidade do Porto, Rua do Campo Alegre, s/n, 4169-007 Porto, Portugal

<sup>8</sup> Department of Astronomy, University of Maryland, College Park, MD 20742, USA

<sup>9</sup> Department of the Geophysical Sciences, The University of Chicago, Chicago, IL, 60637, USA

<sup>10</sup> Center for Astrophysics | Harvard & Smithsonian, 60 Garden Street, Cambridge, MA 02138, USA

<sup>11</sup> Tsinghua International School, Beijing 100084, People's Republic of China

<sup>12</sup> Hazelwood Observatory, Australia

<sup>13</sup> DTU Space, National Space Institute, Technical University of Denmark, Elektrovej 328, DK-2800 Kgs. Lyngby, Denmark

<sup>14</sup> Centre for Astrophysics, University of Southern Queensland, Toowoomba, QLD, 4350, Australia

<sup>15</sup> Instituto de Astrofísica de Canarias, E-38205 La Laguna, Tenerife, Spain

<sup>16</sup> Departamento de Astrofísica, Universidad de La Laguna, E-38206 La Laguna, Tenerife, Spain

<sup>17</sup> Caltech/IPAC-NASA Exoplanet Science Institute, Pasadena, CA, USA

<sup>18</sup> Department of Astronomy, Yale University, New Haven, CT 06511, USA

<sup>19</sup> Division of Geological and Planetary Sciences, California Institute of Technology, 1200 E California Boulevard, Pasadena, CA 91125, USA

<sup>20</sup> Cahill Center for Astronomy & Astrophysics, California Institute of Technology, Pasadena, CA 91125, USA

<sup>21</sup> Department of Physics & Astronomy, University of California Los Angeles, Los Angeles, CA 90095, USA

<sup>22</sup> Department of Physics & Astronomy, University of California Irvine, Irvine, CA 92697, USA

<sup>23</sup> Department of Astronomy and Astrophysics, University of California, Santa Cruz, CA 95064, USA

<sup>24</sup> Department of Earth and Planetary Sciences, University of California Riverside, 900 University Avenue, Riverside, CA 92521, USA

<sup>25</sup> Department of Physics & Astronomy, University of Kansas, 1082 Malott, 1251 Wescoe Hall Drive, Lawrence, KS 66045, USA

<sup>26</sup> Department of Astronomy, Columbia University, 550 West 120th Street, New York, NY, USA

<sup>27</sup> Department of Physics and Kavli Institute for Astrophysics and Space Research, Massachusetts Institute of Technology, Cambridge, MA 02139, USA

<sup>28</sup> NASA Ames Research Center, Moffett Field, CA 94035, USA

<sup>29</sup> SETI Institute, Mountain View, CA 94043, USA

<sup>30</sup> NASA Goddard Space Flight Center, Exoplanets and Stellar Astrophysics Laboratory (Code 667), Greenbelt, MD 20771, USA

<sup>31</sup> Department of Earth, Atmospheric, and Planetary Sciences, Massachusetts Institute of Technology, 77 Massachusetts Avenue, Cambridge, MA 02139, USA

<sup>32</sup> Department of Aeronautics and Astronautics, Massachusetts Institute of Technology, 77 Massachusetts Avenue, Cambridge, MA 02139, USA

<sup>33</sup> Department of Astrophysical Sciences, Princeton University, 4 Ivy Lane, Princeton, NJ 08544, USA

Received 2021 December 1; revised 2022 January 6; accepted 2022 January 7; published 2022 February 9

## Abstract

Giant planets on short-period orbits are predicted to be inflated and eventually engulfed by their host stars. However, the detailed timescales and stages of these processes are not well known. Here, we present the discovery of three hot Jupiters ( $P < 10$  days) orbiting evolved, intermediate-mass stars ( $M_* \approx 1.5 M_\odot$ ,  $2 R_\odot < R_* < 5 R_\odot$ ). By combining TESS photometry with ground-based photometry and radial velocity measurements, we report masses and radii for these three planets of between 0.4 and 1.8  $M_J$  and 0.8 and 1.8  $R_J$ . TOI-2337b has the shortest period ( $P = 2.99432 \pm 0.00008$  days) of any planet discovered around a red giant star to date. Both TOI-4329b and TOI-2669b appear to be inflated, but TOI-2337b does not show any sign of inflation. The large radii and relatively low masses of TOI-4329b and TOI-2669b place them among the lowest density hot Jupiters currently known, while

<sup>34</sup> Kalbfleisch Fellow.

<sup>35</sup> NSF Graduate Research Fellow.

<sup>36</sup> NHFP Fellow.

<sup>37</sup> 51 Pegasi b Fellow.

<sup>38</sup> NSF Astronomy and Astrophysics Postdoctoral Fellow.



Original content from this work may be used under the terms of the [Creative Commons Attribution 4.0 licence](https://creativecommons.org/licenses/by/4.0/). Any further distribution of this work must maintain attribution to the author(s) and the title of the work, journal citation and DOI.

TOI-2337b is conversely one of the highest. All three planets have orbital eccentricities of below 0.2. The large spread in radii for these systems implies that planet inflation has a complex dependence on planet mass, radius, incident flux, and orbital properties. We predict that TOI-2337b has the shortest orbital decay timescale of any planet currently known, but do not detect any orbital decay in this system. Transmission spectroscopy of TOI-4329b would provide a favorable opportunity for the detection of water, carbon dioxide, and carbon monoxide features in the atmosphere of a planet orbiting an evolved star, and could yield new information about planet formation and atmospheric evolution.

*Unified Astronomy Thesaurus concepts:* [Exoplanet astronomy \(486\)](#); [Star-planet interactions \(2177\)](#); [Stellar evolution \(1599\)](#)

## 1. Introduction

Exoplanets have been known around evolved stars at orbital separations of  $>1$  au for decades (e.g., Hatzes et al. 2003). However, planets at smaller separations were expected to be engulfed due to angular momentum exchange through tides (Hut 1981; Villaver & Livio 2009). Thus less than a decade ago, no planets were known on orbits smaller than 1 au around stars with radii greater than  $3 R_{\odot}$  and masses above  $1 M_{\odot}$  (Schlaufman & Winn 2013; Villaver et al. 2014).

This changed with the discovery of Kepler-91b, a Jupiter-sized planet orbiting a  $6.3 R_{\odot}$  star every 6.25 days (Lillo-Box et al. 2014; Barclay et al. 2015). Subsequent discoveries with the NASA Kepler Mission and its extension, K2, have proven planets can survive at short periods around evolved stars (Almenara et al. 2015; Van Eylen et al. 2016; Chontos et al. 2019). Detailed stellar characterization through asteroseismology of these systems revealed that planets can interact with their host star, potentially becoming re-inflated at late times (Grunblatt et al. 2016, 2017). Occurrence studies have now revealed that hot Jupiters are equally common around main-sequence stars and low-luminosity red giant branch stars (Howard et al. 2012; Grunblatt et al. 2019). However, a number of questions about the origins of these systems remain unanswered. Were these planets hot Jupiters before their host stars evolved off the main sequence, or cold Jupiters that have migrated inwards thanks to tidal interactions with their post-main-sequence host stars (Grunblatt et al. 2018)? Are the atmospheres of these planets undergoing stripping (e.g., Spake et al. 2018; Bell et al. 2019)? Other observable properties of red giants are said to be potential signs of planet engulfment (Carlberg et al. 2013; MacLeod et al. 2018; Soares-Furtado et al. 2021). Do these correlate strongly with hot Jupiter occurrence? Can we detect clear evidence for orbital decay (Yee et al. 2020; Turner et al. 2021), planetary atmospheric evolution (Baxter et al. 2021), or exchange of material between star and planet (e.g., Rappaport et al. 2013), to constrain the death of a planetary system?

The Transiting Exoplanet Survey Satellite (TESS; Ricker et al. 2014) is enabling the discovery of a predicted  $\sim 14,000$  planets (Sullivan et al. 2015; Barclay et al. 2018). During its nominal 2 yr mission, the space telescope observed most of its targets in the Full Frame Images (FFIs) with a 30 minutes observing cadence, and has completed at least one year of observations in each of the northern and southern hemispheres. Each year was split into 13 observing sectors that stretched from the ecliptic pole to the ecliptic plane, moving every  $\sim 27$  days. Targets near the ecliptic pole were observed in multiple sectors, in some cases providing a full year of photometry, while targets closer to the ecliptic plane were observed in fewer sectors. According to the NASA Exoplanet Science Institute (NExSci) archive,<sup>34</sup> TESS has already led to the discovery of 100+ confirmed planets and

4000+ project candidates (Guerrero et al. 2021). Of the planets confirmed to date, only a handful orbit evolved host stars; among those is TOI-197b, the first TESS planet discovery orbiting an evolved host with an asteroseismic detection (Huber et al. 2019). There have also been detections of planets orbiting subgiant stars for which asteroseismic detections were not possible (e.g., Nielsen et al. 2019; Wang et al. 2019; Eisner et al. 2020; Saunders et al. 2022).

Through our programs to identify and confirm planets around evolved stars using TESS FFIs (Guest Investigator programs GO22102, GO3151, and GO4179), we have begun successfully identifying new planet candidates and confirming new planetary systems. The first planet found in our survey was observed in both 30 minutes and 2 minutes cadence TESS data (Saunders et al. 2022). Here, we present three additional planets confirmed by our survey, all found in 30 minutes cadence FFI TESS data. These planets are among the shortest-period planets found around evolved host stars, and thus provide new constraints on the process of planetary inspiral and engulfment. Here, we present analysis of the currently available data, and discuss what future observations from TESS and other ground-based and space-based facilities of these systems may reveal about star-planet interaction and evolution.

## 2. Observations

### 2.1. TESS Photometry

TOI-2337b, TOI-4329b, and TOI-2669b were discovered as part of our survey identifying new planets around evolved host stars. Using the TESS Input Catalog (TICv8; Stassun et al. 2019), we made cuts based on color, magnitude, and Gaia parallax in order to limit our sample to evolved stars. We developed the `giants`<sup>35</sup> Python package for accessing, detrending, and searching TESS observations for periodic transit signals (Saunders et al. 2022). The details of how this pipeline processes TESS full frame image data are described in detail in Saunders et al. (2022). We present the `giants` light curves for these targets in Figure 1.

We used our `giants` pipeline to produce TESS light curves for as many red giant branch stars with TESS magnitude  $m_T < 13$  as possible. We produced approximately 540,000 light curves from the first two years of data from the TESS Mission. We then performed an automated BLS search on these targets, and produced summary plots using the BLS output as well as TIC information and the pixel cut out. These summary plots were then visually inspected, during which all three of these candidates were flagged for potential rapid follow-up.

Thirteen sectors of data were available for TOI-2337b at the conclusion of the TESS prime mission, during which over 100

<sup>34</sup> [nexsci.caltech.edu](https://nexsci.caltech.edu)

<sup>35</sup> <https://github.com/nksaunders/giants>

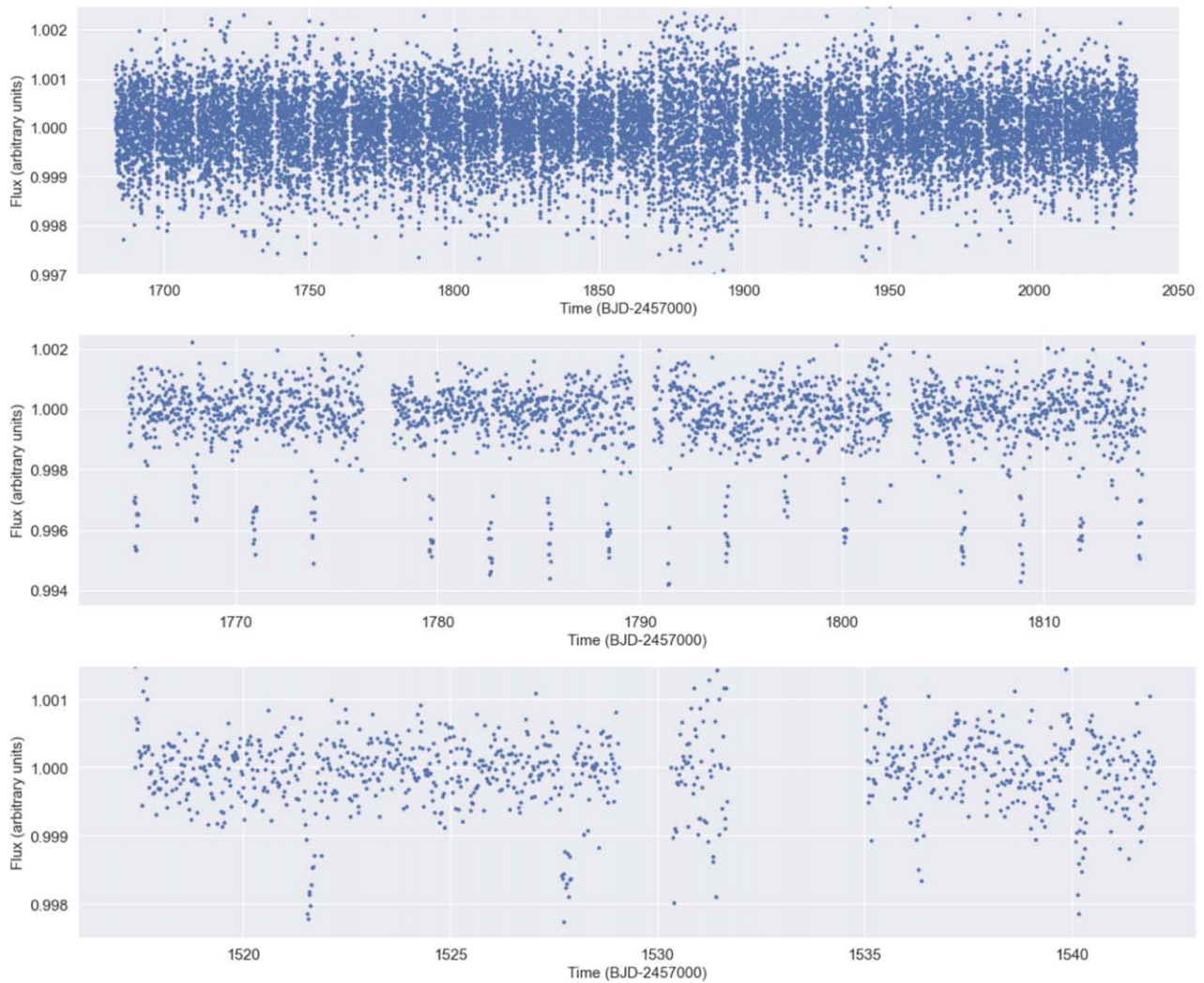


**Figure 1.** Full TESS prime mission light curves of TOI-2337, TOI-4329, and TOI-2669 (from top to bottom, respectively). Light curves for all stars in this study were produced through the `giants` pipeline. Additional data have since been acquired at 10 minutes cadence for TOI-2337 and TOI-2669, supporting the previous transit detections.

transits were observed. Additional data are currently being taken for this target as part of the TESS extended mission. Conversely, TOI-4329b was only observed in three sectors of the TESS prime mission. The last sector of data for TOI-4329b also appeared to be corrupted when producing our `giants` light curve, and thus only 15 transits were observed. TOI-2669b was only observed for one sector of the TESS prime mission, during which three planet transits were observed. Four additional planet transits were observed during one additional sector of observation in the TESS extended mission, which we include in our full planet characterization in Section 4.

To ensure our transit depths from the `giants` pipeline were reliable, we also generated a TESS light curve for each of TOI-2337, TOI-4329, and TOI-2669 using the `eleanor` pipeline to access FFI data calibrated by the TESS Science Processing Operations Center (Jenkins et al. 2016; Feinstein et al. 2019), and performed our transit search on the `eleanor`-corrected light curves. We additionally performed our own systematics removal on the `eleanor`-corrected light curves through a modified version of the `giants` pipeline to independently verify the presence of transits (Saunders et al. 2022). When we applied the same BLS search to our corrected light curve, we

identified an eclipse signal with the same period as found in the `eleanor` light curves, and transit depths that agreed within  $\approx 10\%$  or less for TOI-2337b and TOI-2669b.

Due to a nearby star with a  $\Delta m_V = 3.5$  falling onto the same TESS pixel as TOI-4329b, flux contamination is a larger concern for this system than for TOI-2337b or TOI-2669b, resulting in transit depths between pipelines that disagree by  $>30\%$ . In order to understand the effect of flux contamination on our estimated transit depth, we compared our `giants` light curve to the QLP light curve produced by the MIT team. We display the phase-folded light curves from `giants` along with the QLP light curve, illustrating both the “KSPSAP FLUX” and “SAP FLUX” values produced by their pipeline in Figure 2. As the “KSPSAP FLUX” pipeline is smoothed using a window length of 0.3 day, it is likely that the transit of TOI-4329b could have been diluted. This hypothesis is supported by the ramping before and after transit that is only seen in the “KSPSAP FLUX” light curve but not in the “SAP FLUX” and `giants` light curves. We illustrate the differences between these light curves in Figure 2, and discuss the implications for our determination of the radius of TOI-4329b in Section 4.



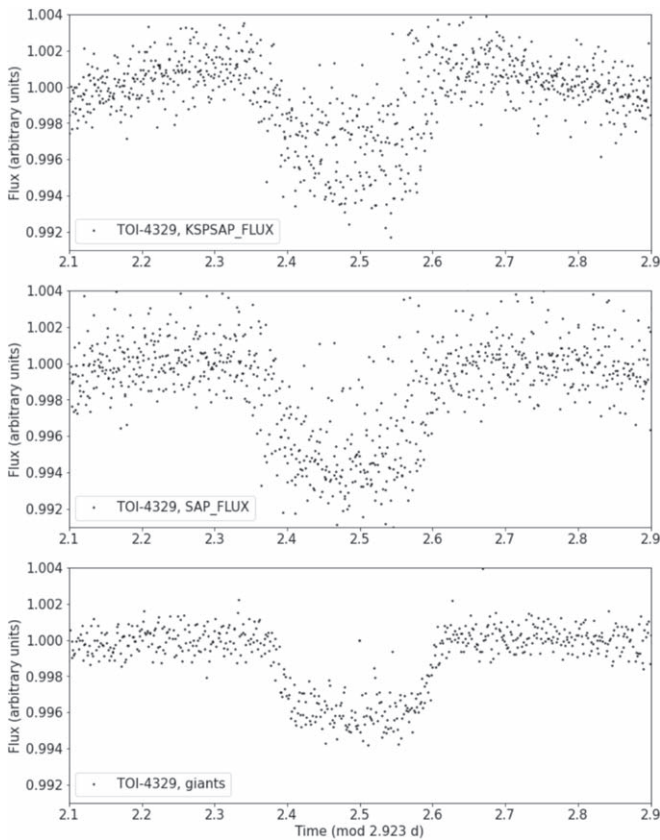


**Figure 2.** Phase-folded light curves of TOI-4329 using the QLP “KSPSAP FLUX,” “SAP FLUX,” and *giants* fluxes (from top to bottom, respectively). Clear differences in transit depth and shape and light-curve scatter can be seen between the different light curves.

## 2.2. Radial Velocity Measurements

Radial velocity (RV) observations were taken with the HIRES spectrograph on the Keck I telescope on Maunakea, Hawaii (Vogt et al. 1994). HIRES has a resolving power of  $R \approx 120,000$  and wavelength coverage between  $\sim 350$  and  $\sim 620$  nm. Seven RV measurements were taken of TOI-2337 between 2020 August 1 and September 2, 9 RV measurements were taken of TOI-4329 between 2020 August 7 and December 25, and 10 RV measurements of TOI-2669 were taken between 2020 December 31 and 2021 June 13.

Additional RV observations of TOI-2337 were taken with the FIES spectrograph on board the Nordic Optical Telescope on La Palma, Canary Islands (Telting et al. 2014). FIES has a resolving power of  $R \approx 65,000$  and wavelength coverage between  $\sim 370$  nm and  $\sim 730$  nm. Fourteen observations with FIES were made between 2020 September 2 and October 25.

Additional observations of TOI-2669 were taken using the CHIRON spectrograph on board the 1.5 m SMARTS telescope in Chile (Tokovinin et al. 2013) between 2020 November and 2021 May. Data were obtained in slicer mode, which uses a fiber feed and an image slicer to yield  $R \approx 79,000$  over the spectral range 410 nm to 880 nm. The spectra were extracted as per Paredes et al. (2021). Radial velocities were measured from the spectra via a cross correlation between each epoch against a median-combined observed template. Approximate absolute velocities were first derived from each spectrum as per Zhou et al. (2020). The spectra were then median combined with the approximate velocities removed to form a master template

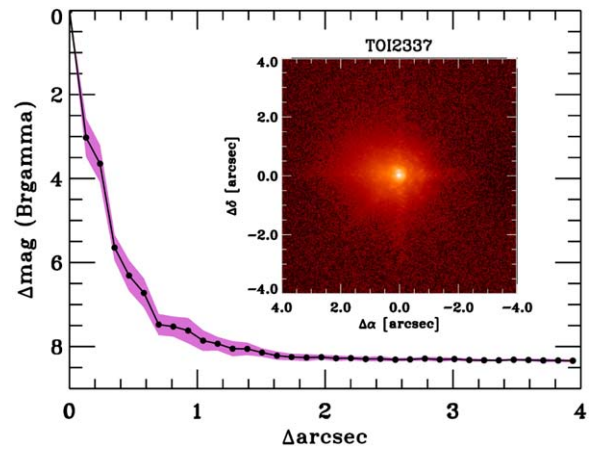


**Figure 3.** Contrast curve for TOI-2337, with the corresponding ground-based adaptive optics image shown in the inset. TOI-2337 appears to be a single star based on this analysis.

spectrum. Cross correlations were performed over the wavelength range of 410–620 nm, with the Balmer, sodium, and telluric regions masked out.

## 2.3. Ground-based Imaging of TOI-2337

TOI-2337 was also observed by the PHARO instrument on the 5 m Hale telescope at the Palomar Observatory in California. Observations were taken on 2021 June 24 in the  $\text{Br}\gamma$  filter near  $2.2 \mu\text{m}$ . The contrast curve for these observations can be seen in Figure 3, which shows the detection limits in contrast ( $\Delta m$ ) versus angular separation from the point-spread function center in arcseconds for the filter wavelength. The inset image is the speckle auto-correlation function for the observation. No additional stars can be identified within  $4''$  of our target, as shown in the inset image. Although another faint star can be identified approximately  $7''$  southeast of our target, this star has an inconsistent proper motion with our target (Gaia Collaboration et al. 2018) and thus is likely not associated with our target, and is too faint to cause significant transit dilution.

While TOI-4329 and TOI-2669 do not have high-resolution imaging results, the Gaia astrometric noise metric RUWE is low (0.91 and 1.04, respectively), indicative that the stars are not in wide binary systems that could be resolved by Gaia photometry. Additionally, no evidence of a spectroscopic binary can be seen in the spectra of these stars, placing limits on close binarity for these stars. The radial velocity measurements of these systems do not show any significant linear or quadratic trends with time, suggesting these stars are single and not part of a binary system.

## 2.4. Ground-based Photometry of TOI-2337

TOI-2337 was also observed by the Las Cumbres Observatory Global Telescope (LCOGT) 1 m telescope at McDonald Observatory in West Texas on 2021 June 12 and August 22 and by the LCOGT 1 m telescope at Teide Observatory in the Canary Islands between 2021 August 1 and August 22.

Observations from the Teide Observatory captured multiple ingresses of transits, while observations from McDonald Observatory were able to capture the egresses of multiple transits. Observations were scheduled using the TESS Transit Finder, which is a customized version of the Tapir software package (Jensen 2013). The images were calibrated by the

**Table 1**  
Stellar Properties Derived from an isoclassify Fit to HIRES Spectroscopic Observations

<i>Target IDs</i>			
TOI	2337	4329	2669
TIC	230001847	256722647	348835438
TYC	4217-01423-1		5456-00076-1
2MASS	J19222878+6051140	J21581534+7107538	J08585340-1318450
Gaia DR2	2239684947894267392	2224458777730383616	5735664051960550144
<i>Coordinates</i>			
R.A. (J2015.5)	19:22:28.77	21:58:15.34	08:58:53.43
Decl. (J2015.5)	60:51:14.05	71:07:53.78	-13:18:45.29
<i>Characteristics</i>			
TESS mag	11.23	11.88	9.99
Radius $R_*$ ( $R_\odot$ )	$3.220 \pm 0.062 R_\odot$	$2.31 \pm 0.03 R_\odot$	$4.10 \pm 0.04 R_\odot$
Mass $M_*$ ( $M_\odot$ )	$1.325 \pm 0.118 M_\odot$	$1.538 \pm 0.049 M_\odot$	$1.19 \pm 0.16 M_\odot$
$T_{\text{eff}}$ (K)	$4780 \pm 100$ K	$6000 \pm 100$ K	$4800 \pm 100$ K
$\log(g)$ (dex)	$3.50 \pm 0.06$ dex	$3.90 \pm 0.03$ dex	$3.29 \pm 0.07$ dex
[Fe/H] (dex)	$0.39 \pm 0.06$ dex	$0.29 \pm 0.06$ dex	$0.1 \pm 0.06$ dex
Age (Gyr)	$4.9 \pm 1.8$ Gyr	$2.39 \pm 0.45$ Gyr	$5.9 \pm 3.0$ Gyr
Density $\rho_*$ ( $\rho_\odot$ )	$0.039 \pm 0.005 \rho_\odot$	$0.127 \pm 0.006 \rho_\odot$	$0.018 \pm 0.003 \rho_\odot$

standard LCOGT BANZAI pipeline (McCully et al. 2018), and photometric data were extracted with AstromageJ (Collins et al. 2017). A fit to the ground-based data using the TESS determined ephemeris finds a fractional transit depth  $\delta \approx 800$  ppm, orbital period  $P = 2.9943209 \pm 0.0000387$  days (using the reference epoch we derive from the TESS data), and time of transit  $T_0 = 2,459,033.36898 \pm 0.00267$ , within  $1\sigma$  of values extracted from our simultaneous fit to the TESS giants light curve and RV data (see Table 2). The observed ingresses and egresses of the planet transit are within 0.05 day of the expected times, corresponding to a transit ephemeris uncertainty  $\Delta T_c = 40$  minutes, placing constraints on the rate of orbital decay of this system that are discussed in more detail in Section 8.

### 3. Host Star Characterization

#### 3.1. High-resolution Spectroscopy

We used SpecMatch to measure the metallicity, surface gravity, and effective temperature of the host stars from our HIRES spectra (Petigura 2015). We then used isoclassify (Huber et al. 2017) to combine TICv8 and spectroscopic information to determine stellar properties, listed in Table 1.

Figure 4 shows a Hertzsprung–Russell (HR) diagram with evolutionary tracks downloaded from the MESA Isochrones and Stellar Tracks (MIST; Paxton et al. 2011; Choi et al. 2016; Dotter 2016). As all three host stars have roughly the same mass and metallicity ( $M_* \approx 1.5 M_\odot$ ,  $[\text{Fe}/\text{H}] \approx 0.25$  dex), we suggest that these systems may represent an evolutionary sequence for post-main-sequence, intermediate-mass stars. We find that both TOI-2337 and TOI-2669 lie on the red giant branch, while TOI-4329 lies at an earlier subgiant stage of evolution.

#### 3.2. Asteroseismology of TOI-2669

Asteroseismology is the study of oscillations in stars. In particular, solar-like oscillations can be used to probe the internal structure and fundamental physical properties of a star (Kjeldsen & Bedding 1995). These oscillations can be seen and measured in the power spectrum of a light curve produced from

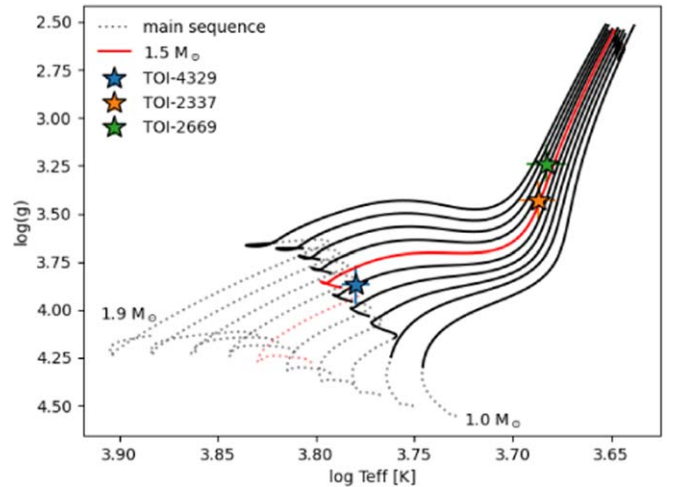


**Figure 4.** Position of TOI-2337, TOI-4329, and TOI-2669 on an HR diagram. All host stars have evolved off of the main sequence onto the subgiant and red giant branch. We also illustrate MIST evolutionary tracks of  $1\text{--}2 M_\odot$ ,  $+0.25$   $[\text{Fe}/\text{H}]$  dex stars in  $0.1 M_\odot$  increments for reference. We have highlighted a MIST evolutionary track for a  $1.5 M_\odot$ ,  $[\text{Fe}/\text{H}] = 0.25$  dex star in red, illustrating the evolutionary sequence probed here.

30 minutes cadence full frame image TESS data of a red giant star (Aguirre et al. 2020; Grunblatt et al. 2021). Figure 5 illustrates the power spectrum of the second sector of TESS data for TOI-2669, where the expected frequency of excess power has been labeled by a gray dashed line. To perform a rigorous asteroseismic analysis, we use the pySYD package built on the SYD asteroseismic pipeline (Huber et al. 2009; Chontos et al. 2021). We identify a  $\nu_{\text{max}}$  value of  $210 \pm 30 \mu\text{Hz}$  for this star, corresponding to a  $\log(g) \approx 3.2$ , in agreement with the TICv8 and isoclassify-determined values. However, the signal-to-noise ratio of the detection is currently too low to determine an accurate  $\Delta\nu$  value. Thus we validate our stellar mass and radius using these asteroseismic parameters, but use the isoclassify-derived stellar parameters to determine planet mass and radii for TOI-2669b. Additional asteroseismic studies with TESS will improve methods for identifying and

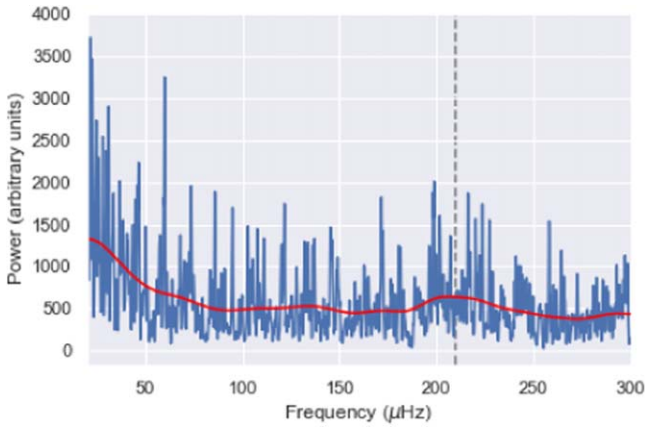


**Figure 5.** Power density spectrum of the 10 minutes cadence data of TOI-2669, where the data are shown in blue, a smoothed power spectrum is shown in red, and the expected maximum power of oscillation  $\nu_{\max}$  is labeled by the gray dashed line. A power excess is slightly significant in the data near this value as measured with `pySYD`.

measuring asteroseismic signals with limited time series data (e.g., Mackereth et al. 2021; Hon et al. 2021).

## 4. Planet Characterization

### 4.1. Model Fit

We used the `exoplanet` Python package to simultaneously fit a model to the photometry and radial velocity observations (Foreman-Mackey et al. 2020). The data input to our model were all radial velocity observations and all sectors of TESS FFI photometry available from the first three years of the TESS Mission. Our model used stellar parameters derived using `isoclassify` (Huber et al. 2017) with Gaia parallax, and input effective temperature ( $T_{\text{eff}}$ ) and metallicity estimated from spectral observations taken at the Keck Observatory. These model input parameters can be found in Table 1.

Our initial choices of planet period and depth were taken from the BLS search determined values produced during the transit search described in Section 2.2. For limb darkening, we use the quadratic model prescribed by Kipping (2013) to provide a two-parameter model with uninformative sampling. We parameterize eccentricity using the single-planet eccentricity distribution of Van Eylen et al. (2019).

We present our best-fit models to the light curve and radial velocity data for TOI-2337 in Figure 6 and Table 2. We investigate the additional out-of-transit light-curve variability of TOI-2337 in Figure 7. We then present our best-fit models to the light curve and radial velocity data of TOI-4329 and TOI-2669 in Figures 8 and 9 and Tables 3 and 4, respectively. We find that despite the similar masses we have measured for the host stars in these systems, the planet masses, radii, and densities cover a wide range that is not clearly correlated with stellar properties.

For TOI-4329b, we performed a joint radial velocity and transit fit using the “KSP SAP,” “SAP FLUX,” and `giants` flux values. We find a planet radius of  $1.37 \pm 0.07 R_J$  using the `giants` light curve,  $1.60 \pm 0.07 R_J$  using the “SAP FLUX” light curve, and  $1.41 \pm 0.07 R_J$  using the “KSPSAP FLUX” light curve. We find a maximum range in planet radii determined by these fits of  $0.24 R_J$ , significantly larger than the uncertainty in planet transit depth estimated from any fit to the available data. Thus, we assume that flux contamination

must be the dominant source of uncertainty in planet radius determination for this system. As the difference between median planet radius reported between the two light curves is significantly larger than the errors on planet radius from either individual light curve, we add the statistical errors of each light-curve fit in quadrature and add those to one half the difference between median values to get a planet radius uncertainty of  $0.19 R_J$  for TOI-4329b. Future observations with facilities with better resolution capable of using smaller photometric apertures, such as those used by the LCOGT, will confirm the true transit depth of this system, more precisely constraining the radius of TOI-4329b.

### 4.2. BEER Modeling with `starry`

The folded light curve of TOI-2337 revealed not only a transit signal, but also corresponding out-of-transit variability at the same orbital period. To model the out-of-transit phase curve variations in this star, we adopt a beaming, ellipsoidal variability and reflection (BEER) model (Faigler & Mazeh 2011) to account for reflection of light off of the planet, ellipsoidal variations in the star, and Doppler beaming of the light assisted by the planet. These effects can be modeled as trigonometric functions:

$$M(t) = a_0 + \alpha \cos\left(\frac{2\pi}{P_{\text{orb}}}t\right) + \beta \cos\left(\frac{2\pi}{P_{\text{orb}}/2}t\right) + \gamma \sin\left(\frac{2\pi}{P_{\text{orb}}}t\right), \quad (1)$$

where  $\alpha$  represents the reflection brightness,  $\beta$  represents the amplitude of the ellipsoidal variability, and  $\gamma$  represents the Doppler beaming strength. We find that we can produce a better fit to the data by including significant ellipsoidal variability in our model. Following the formulation of Shporer (2017), we expect the semi-amplitude of ellipsoidal variability  $A_{\text{ellip}}$  can be estimated using

$$A_{\text{ellip}} \propto \frac{M_p}{M_*} \left(\frac{R_*}{a}\right)^3. \quad (2)$$

We model the phase curve variability of this system following the hot Jupiter phase curve example of Luger et al. (2018) with the `starry` package. This model allows us to map the surfaces of both the host star and exoplanet as a sum of spherical harmonics, resulting in a flux model that is equivalent to the BEER model described above. This model also allows us to fit for the offset in the peak flux of the sinusoidal or spherical harmonic components of the flux, allowing for additional flexibility not accessible with a pure BEER model as described above. For our spherical harmonic model, we include a dipole and quadrupole mode at the orbital phase of the planet, which is equivalent to the reflection and ellipsoidal variation terms in the above equation. As the Doppler beaming term we expect from this system is  $<10$  ppm (as determined by Equation (4) in Shporer 2017), we do not fit for it in our model. We then fit for the coefficients of the dipole and quadrupole terms, as well as an overall variability strength and phase offset term, to model the light curve of TOI-2337b, folded at the planet orbital phase listed in Table 2 and binned the folded light curve with a bin size of 48 points. We illustrate our best-fit model and  $1\sigma$  confidence intervals in Figure 7.



**Table 2**  
Fit and Derived Parameters for TOI-2337b

Parameter	Prior	Value
<i>Transit Fit Parameters</i>		
Orbital period $P_{\text{orb}}$ (days)	$\log \mathcal{N}[2.9943, 0.0015]$	$2.99432 \pm 0.00008$ days
Transit epoch $t_0$ (BJD - 2,457,000)	$\mathcal{N}[1793.80652, 1.0]$	$1793.828 \pm 0.003$
Impact parameter $b$	$P_{\beta}(e \in [0, 1])^a$	$0.52 \pm 0.08$
Eccentricity $e$	single-planet dist. from Van Eylen et al. (2019)	$0.019 \pm 0.017$
Argument of periastron $\Omega$	$\mathcal{U}[-\pi, \pi]$	$-0.341 \pm 1.228$
Limb-darkening coefficient $q_1$	$[0, 2]^b$	$0.460 \pm 0.261$
Limb-darkening coefficient $q_2$	$[-1, 1]^b$	$0.322 \pm 0.346$
<i>Radial Velocity Fit Parameters</i>		
Semi-amplitude $K$ ( $\text{m s}^{-1}$ )	$\mathcal{U}[0, 500]$	$192.2 \pm 2.6$
<i>Derived Physical Parameters</i>		
Planet radius $R_p$ ( $R_{\oplus}$ )	$\mathcal{U}[0, 3]$	$0.9 \pm 0.1 R_J$
Planet mass $M_p$ ( $M_J$ )	$\mathcal{U}[0, 300]$	$1.60 \pm 0.15 M_J$

**Notes.**

<sup>a</sup> This parameterization is described by the Beta distribution in Kipping (2013).

<sup>b</sup> Distributions follow correlated two-parameter quadratic limb-darkening law from Kipping (2013).

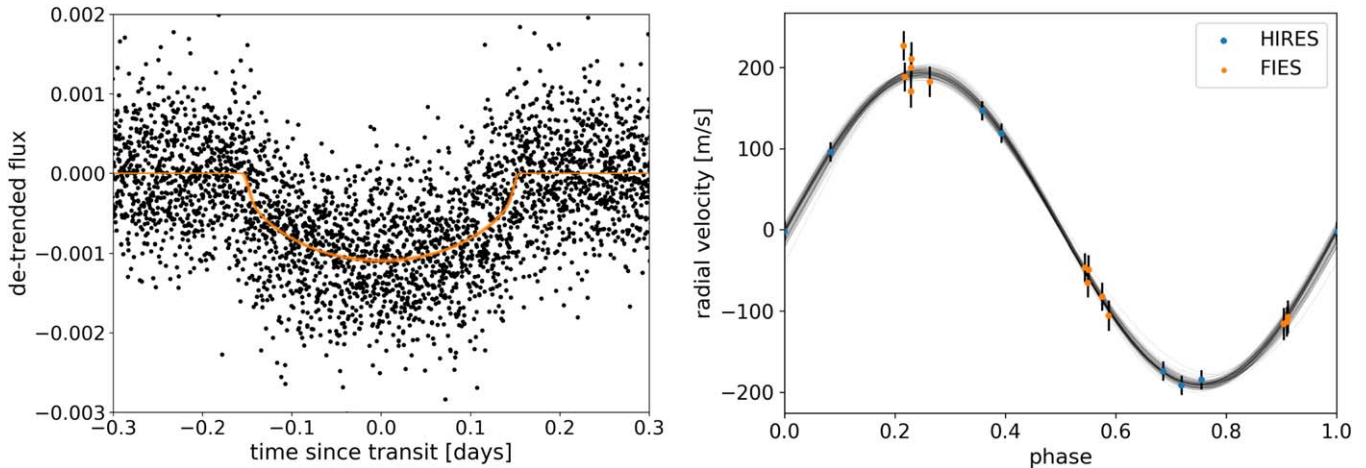


**Figure 6.** Left: the flux light curve of TOI-2337 folded at a period of  $2.99432 \pm 0.00008$  days. The detrended photometry is shown in black with the binned photometry overplotted in orange. Right: all radial velocity observations of TOI-2337b used in this analysis where the time axis has been folded at the orbital period of the planet. Observations come from the Nordic Optical Telescope in La Palma (orange) and the Keck I telescope on Maunakea (blue).

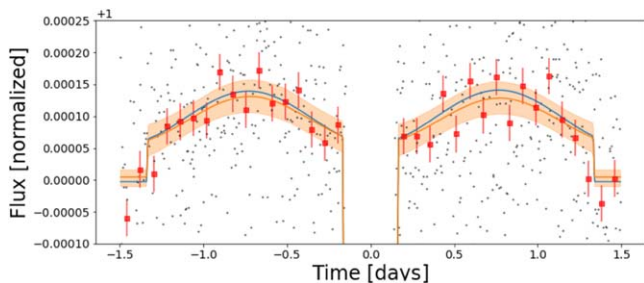


**Figure 7.** The flux light curve of TOI-2337 folded at a period of 2.99432 days, highlighting the out-of-transit variability. The phase-folded, binned photometry is shown as black points. The initial *starry* model is shown in blue, and the best-fit model is shown in orange, with  $1\sigma$  confidence intervals highlighted. Ellipsoidal variation dominates the out-of-transit phase curve variability.

We measure the dipole coefficient to be consistent with 0 and a quadrupole coefficient corresponding to a semi-amplitude of  $\approx 55$  ppm in the TESS *giants* light curve. Assuming a model for ellipsoidal variation following the formulation of

Shporer (2017), we expect the ellipsoidal variation to be most strongly influenced by the scaled orbital separation of the system, as mentioned above. Extrapolating from the measured ellipsoidal variability of other TESS systems (Wong et al. 2020, 2021), we predict an ellipsoidal semi-amplitude of  $75 \pm 15$  ppm for this system, in good agreement with our detection.

A more complicated BEER model that allows for eccentricity may be able to remove some additional noise, but due to the strong constraint on eccentricity from radial velocity follow-up ( $e < 0.05$  at a 95% confidence interval) we do not allow eccentricity in our out-of-transit phase variability model. The strongest out-of-transit phase signal is clearly due to a quadrupole-like variation such as ellipsoidal variability. In addition, we measure a significant offset in phase for the out-of-transit sinusoidal variation. Allowing the ellipsoidal variability to lag the transit in phase produces a better fit to the data.

No significant out-of-transit variability can be seen for TOI-4329b or TOI-2669b. Recent 10 minutes cadence data available

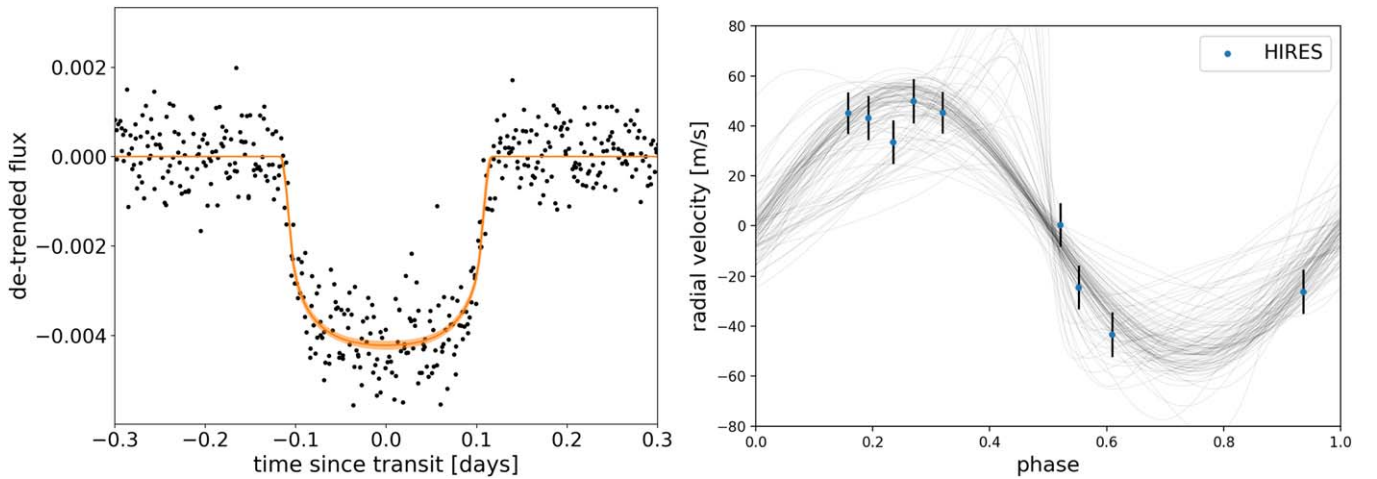


**Figure 8.** Same as Figure 6 for TOI-4329b phase-folded at  $2.9223 \pm 0.00015$  days. Right: observations come from the Keck I telescope on Maunakea.

**Table 3**  
Fit and Derived Parameters for TOI-4329b

Parameter	Prior	Value
<i>Transit Fit Parameters</i>		
Orbital period $P_{\text{orb}}$ (days)	$\log \mathcal{N}[2.923, 0.001]$	$2.9223 \pm 0.00015$
Transit epoch $t_0$ (BJD $- 2,457,000$ )	$\mathcal{N}[1765.067, 0.05]$	$1765.068 \pm 0.002$
Impact parameter $b$	$P_{\beta}(e \in [0, 1])^a$	$0.24 \pm 0.18$
Eccentricity $e$	single-planet dist. from Van Eylen et al. (2019)	$0.068 \pm 0.079$
Argument of periastron $\Omega$	$\mathcal{U}[-\pi, \pi]$	$0.285 \pm 2.120$
Limb-darkening coefficient $q_1$	$[0, 2]^b$	$0.258 \pm 0.165$
Limb-darkening coefficient $q_2$	$[-1, 1]^b$	$0.535 \pm 0.263$
<i>Radial Velocity Fit Parameters</i>		
Semi-amplitude $K$ ( $\text{m s}^{-1}$ )	$\mathcal{U}[0, 300]$	$55.6 \pm 4.1$
<i>Derived Physical Parameters</i>		
Planet radius $R_p$ ( $R_{\oplus}$ )	$\mathcal{U}[0, 3]$	$1.50 \pm 0.19 R_J$
Planet mass $M_p$ ( $M_J$ )	$\mathcal{U}[0, 300]$	$0.45 \pm 0.09 M_J$

**Notes.**

<sup>a</sup> This parameterization is described by the Beta distribution in Kipping (2013).

<sup>b</sup> Distributions follow correlated two-parameter quadratic limb-darkening law from Kipping (2013).

for TOI-2669b gives evidence for a relatively short ( $\approx 6$  hr) transit duration, indicative of either a high impact parameter transit or eccentricity in the planet’s orbit, in agreement with the planet parameters presented here. Combined with previous observations and radial velocity data of TOI-2669b, a low to moderate eccentricity is more likely for this planet ( $e < 0.2$ ), and thus this suggests transit may have a high impact parameter.

### 5. Planet Radius Inflation

Previous to our TESS survey, only seven planets had been confirmed to be transiting evolved ( $T_{\text{eff}} < 6000$  K,  $R > 2 R_{\odot}$ ) stars. These systems showed promise for solving mysteries of late-stage planet inflation and orbital evolution, but small

**Table 4**  
Fit and Derived Parameters for TOI-2669b

Parameter	Prior	Value
<i>Transit Fit Parameters</i>		
Orbital period $P_{\text{orb}}$ (days)	$\log \mathcal{N}[6.203, 0.01]$	$6.2034 \pm 0.0001$
Transit epoch $t_0$ (BJD $- 2,457,000$ )	$\mathcal{N}[1521.56, 0.1]$	$1521.598 \pm 0.009$
Impact parameter $b$	$P_{\beta}(e \in [0, 1])^a$	$0.858 \pm 0.025$
Eccentricity $e$	single-planet dist. from Van Eylen et al. (2019)	$0.09 \pm 0.05$
Argument of periastron $\Omega$	$\mathcal{U}[-\pi, \pi]$	$-1.220 \pm 0.585$
Limb-darkening coefficient $q_1$	$[0, 2]^b$	$0.68 \pm 0.48$
Limb-darkening coefficient $q_2$	$[-1, 1]^b$	$-0.01 \pm 0.41$
<i>Radial Velocity Fit Parameters</i>		
Semi-amplitude $K$ ( $\text{m s}^{-1}$ )	$\mathcal{U}[0, 300]$	$59.6 \pm 3.0$
<i>Derived Physical Parameters</i>		
Planet radius $R_p$ ( $R_{\oplus}$ )	$\mathcal{U}[0, 3]$	$1.76 \pm 0.16 R_J$
Planet mass $M_p$ ( $M_J$ )	$\mathcal{U}[0, 100]$	$0.61 \pm 0.19 M_J$

**Notes.**

<sup>a</sup> This parameterization is described by the Beta distribution in Kipping (2013).

<sup>b</sup> Distributions follow correlated two-parameter quadratic limb-darkening law from Kipping (2013).

numbers and undersampled parameter space have made determining population-wide characteristics difficult. With our additional discoveries (including TOI-2184b from Saunders et al. 2022), our TESS survey has now increased the number of confirmed planets in this population by almost 50%, and has revealed a new regime of short-period hot Jupiters that have not yet inspiralled into their evolved host stars. In addition, our survey has revealed a number of other similar planet candidates that will be suitable for confirmation or at least ground-based follow-up in the near future. Measurements of the masses and eccentricities of these and similar systems will provide new constraints on planetary inflation and evolution, and the rate of inflation in these candidates is already providing new constraints on the mechanisms and timescales for reinflation that were not possible earlier. We illustrate previously known and new



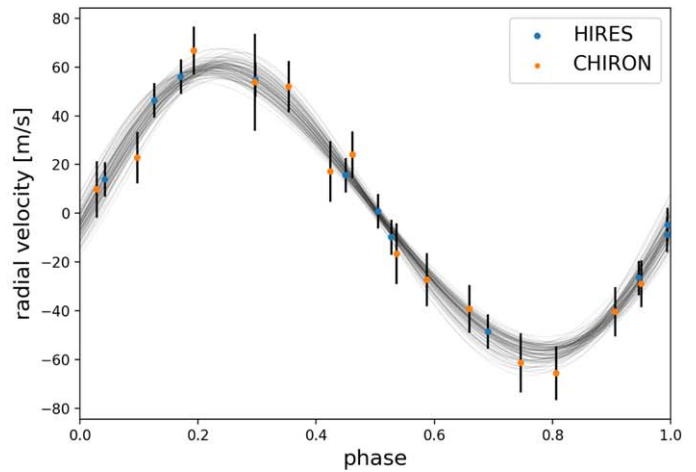
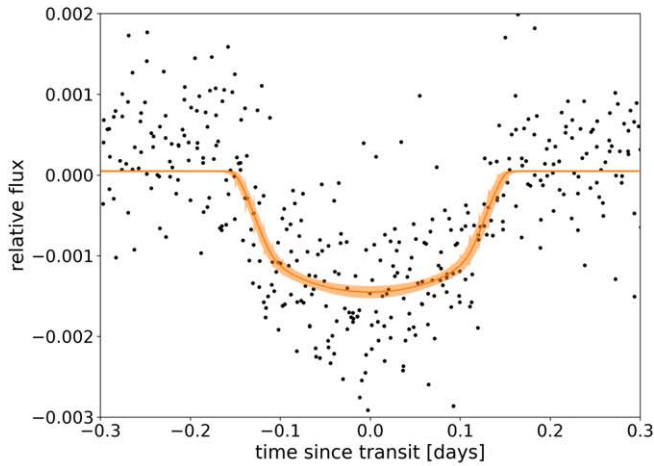


**Figure 9.** Same as Figure 6 for TOI-2669b, phase-folded at  $6.2034 \pm 0.0001$  days. Right: observations come from the Keck I telescope on Maunakea (blue) and the SMARTS-1.5 m telescope at CTIO (orange).

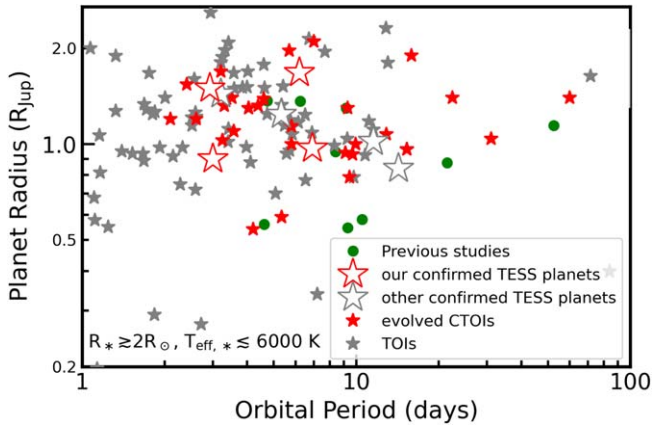


**Figure 10.** Orbital period vs. planet radius for confirmed planets and new candidates transiting evolved ( $R_* > 2 R_\odot$ ,  $T_{\text{eff},*} < 6000$  K) stars. Planets known around evolved stars before the launch of TESS are shown in green. Those confirmed by TESS are shown as the largest symbols. Additional community-flagged planet candidates found by TESS are shown as small red stars, and TESS Objects of Interest (TOIs) are shown in gray.

planets, as well as new planet candidates orbiting evolved stars, in Figure 10.

We illustrate planet radius as a function of incident flux in Figure 11, highlighting the hot Jupiter population. Color indicates planet mass, and we illustrate the planets confirmed by this work as stars and other planets around evolved stars as squares. A strong correlation between incident flux and planet radius can be seen for planets with  $\gtrsim 0.5 M_{\text{Jup}}$  (Demory & Seager 2011; Lopez & Fortney 2016; Thorngren & Fortney 2018; Sestovic et al. 2018). However, a number of outliers to these trends can also be seen—for example, TOI-2337b is the smallest planet known with mass  $> 0.3 M_{\text{Jup}}$  and incident flux  $> 2000 F_\oplus$ , TOI-2184b is similarly significantly underinflated, and TOI-4329b appears somewhat underinflated for its mass and incident flux, while TOI-2669b appears relatively overinflated. This indicates that planet reinflation at late times may be driven by a combination of different factors, but implies that planets can become more inflated at late evolutionary stages (Lopez & Fortney 2016; Grunblatt et al. 2017, 2019). Atmospheric stripping could play a role at such small orbital separations, changing the potential radius and composition of

the planet significantly (Bell et al. 2019; Baxter et al. 2021; Swain et al. 2021).

Relative to other known evolved systems, the incident flux on TOI-2337b is quite high. Thus assuming a direct correlation between planet radius and incident flux, it would be expected that this planet is inflated, yet it is not. As seen in Figure 11, the incident flux received by TOI-2337b is greater than that typically received by similarly sized hot Jupiters—clustered to the left of TOI-2337b—by roughly a factor of 2. On the contrary, both TOI-4329b and TOI-2669b appear to have inflated radii and smaller masses than TOI-2337b.

When taking all evolved systems into account, it appears that they are not evenly distributed among the larger population of inflated Jupiters, but instead seem to prefer relatively low rates of inflation regardless of planet mass. This suggests that for evolved stars, a straightforward mass–radius–flux power-law relation may not be sufficient to describe the observed population, as flux integrated over time and change in flux are also relevant for these systems (Weiss et al. 2013; Sarkis et al. 2021). These flux changes are highly dependent on stellar evolution as well as planetary orbital dynamics. Alternatively, TOI-2337b may simply be an outlier from the typical population of hot Jupiters that are described well by a mass–radius–flux relation, due to mass loss or an unusually massive core.

These systems can be interpreted as evidence for rapid reinflation (Thorngren et al. 2021), which could result in the large difference in planet radii among these particularly high equilibrium temperature planets. The vastly different planet radii could be due to different strengths and depths of heat dissipation processes for the planets studied here (Komacek et al. 2020), but uncertainties in the bulk metallicity and the migration history of these planets may also play a role. The orbits currently observed for these planets may have been reached through circularization induced by stellar evolution (Villaver & Livio 2009; Villaver et al. 2014), which could also result in time-dependent internal heating and radius inflation due to the changing planetary orbit.

## 6. Eccentricity Analysis

Grunblatt et al. (2018) showed that giant planets orbiting giant stars at periods  $< 30$  days have average eccentricities

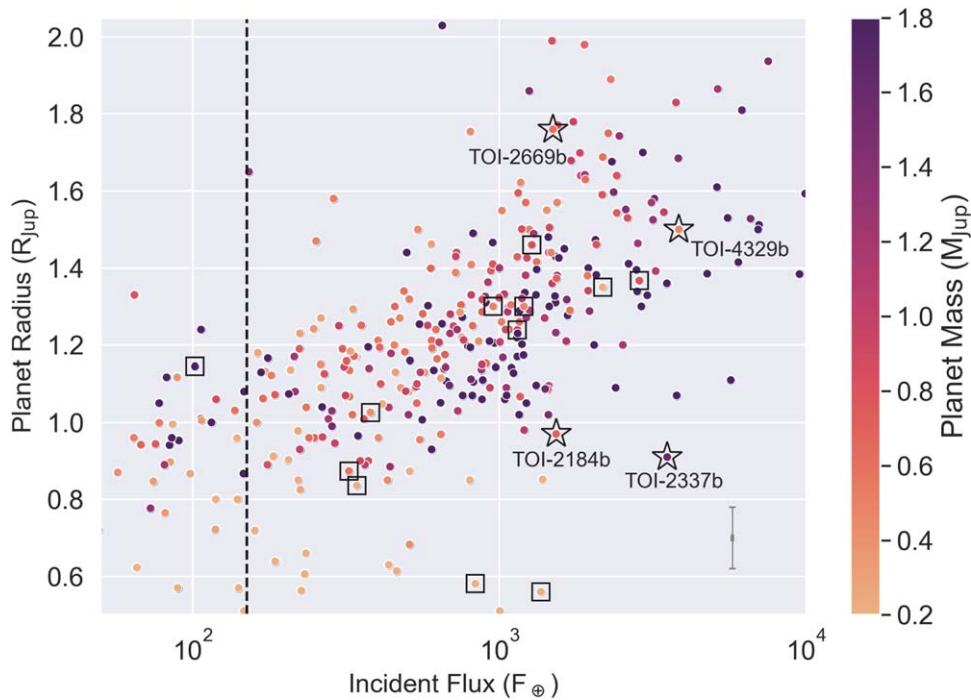


**Figure 11.** Planet radius vs. incident flux for all known hot Jupiters. The black line corresponds to the observed threshold for planet inflation ( $150 F_{\odot}$ ; Demory & Seager 2011). Color corresponds to planet mass. Typical errors for the data are shown by the gray point in the lower right-hand corner of the plot. Previously known evolved ( $R_* > 2 R_{\odot}$ ,  $T_{\text{eff}} < 6000$  K) systems have been highlighted with squares, whereas the new systems confirmed here and TOI-2184b, found in the same planet search, have been highlighted as stars and labeled on this plot. TOI-4329b and TOI-2669b are in good agreement with the larger population trend of known hot Jupiters, while TOI-2337b is an outlier. Evolved systems do not appear to follow a straightforward planet mass–radius–flux relationship, suggesting other factors may be important in the late-stage inflation of planets.

$e > 0.1$ . However, at the shortest orbital periods ( $< 5$  days), even planets around evolved stars appear to have largely circular orbits. The strong upper limits on eccentricities of the orbits in the evolved systems presented here suggests that these systems have largely completed orbital circularization and inspiral as described in Villaver et al. (2014). Constraints on orbital eccentricities will constrain both planet engulfment and stellar structure models (Weinberg et al. 2017; Sun et al. 2018; Soares-Furtado et al. 2021). We find no evidence for significant eccentricity in observations of any three of our systems. Both TOI-2337b and TOI-4329b have eccentricities  $e < 0.05$ , while the longer-period TOI-2669b has an eccentricity potentially inconsistent with zero, yet significantly smaller than 0.15. Given the remarkably short orbital periods of these systems relative to other transiting evolved systems, these results are in strong agreement with the findings of Grunblatt et al. (2018), but a wider range of eccentricities and periods are needed to strongly support the existence of a correlation between orbital eccentricity and period for transiting planets in evolved giant planet systems.

## 7. Potential James Webb Space Telescope Follow-up Observations

Little is understood about the evolution of planetary atmospheres over time, and no observations of planetary atmospheres have been conducted for planets orbiting evolved stars. Due to their particularly short orbits, the systems introduced here are better suited for atmospheric characterization than other planets orbiting evolved stars.

Observations with the James Webb Space Telescope (JWST) will enable the comparison of these evolved planets directly to hot and ultra-hot Jupiters orbiting main-sequence and

pre-main-sequence stars. As it is believed that the hot Jupiters we find on short orbits around evolved stars may have begun their lives on much larger orbits around young stars, comparison between young, main-sequence, and evolved planet transmission spectra could reveal evolution of planetary atmospheres.

We find that TOI-4329b has a transmission spectroscopy metric (TSM; Kempton et al. 2018) value of  $\sim 80$ , making it the best candidate hosted by a  $> 2 R_{\odot}$  star for JWST follow-up. The shallower transit depths of TOI-2337b and TOI-2669b make them less suitable for such follow-up, though TOI-2669b may be amenable to transmission spectroscopy with a precision roughly 70% as good as that of TOI-4329b (TSM of  $\sim 55$ ).

Figure 12 shows the relative transit depth expected to be recovered at different wavelengths by JWST NIRSPEC for TOI-4329b, assuming the default planet atmospheric model of PandExo, with equilibrium chemistry and medium cloud cover and the measured planet mass and temperature (Batalha et al. 2017). The wavelength range probes water and carbon dioxide features, both of which are clearly visible given the relative brightness and precise mass of the planet.

These observations are predicted to constrain the carbon-to-oxygen ratio in the atmosphere of TOI-4329b, informing formation and migration scenarios for these planets as has been done previously for planets orbiting main-sequence stars (Line et al. 2014; Benneke 2015). The relationship between planet mass and atmospheric metallicity of TOI-4329b will be particularly informative in understanding the formation and migration of this system (Welbanks et al. 2019). The differences between the chemical abundances of this planet and of planets in main-sequence systems may reveal how late-stage stellar evolution impacts the evolution of planetary atmospheres.

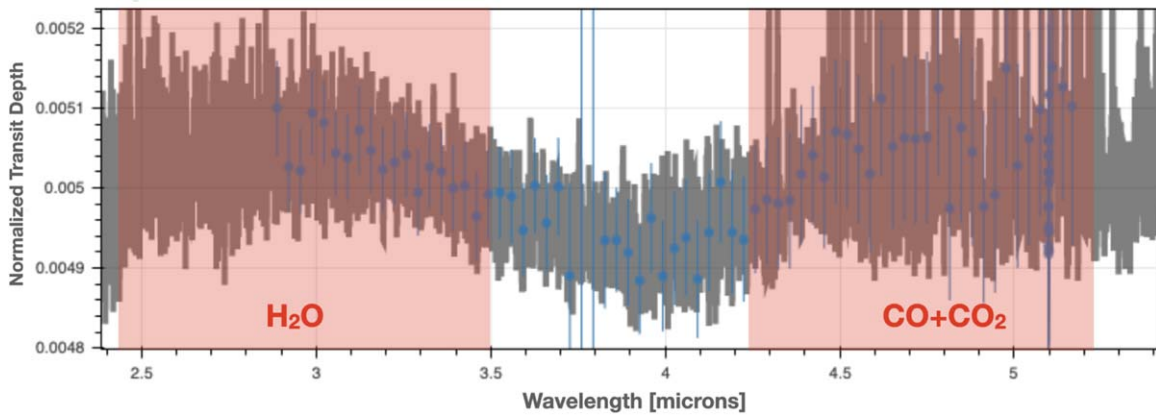


**Figure 12.** Transit depths for TOI-4329b as measured by JWST’s NIRSPEC instrument (blue points) compared to a default planet model atmosphere with equilibrium chemistry and medium cloud cover (gray), at the precision expected for one transit observation (Batalha et al. 2017). The regions of the spectrum sensitive to water and carbon species in the planet’s atmosphere have been highlighted. The strength of these features has implications for the atmospheric composition and mixing in this planet, and the inflation of post-main-sequence planets in general.

Recent observations have suggested a distinction in the atmospheric profiles of hot and ultra-hot Jupiters (Baxter et al. 2021). Additionally, transmission spectra probe atmospheric composition, which can inform what fraction of the atmosphere is primordial versus accreted at later stages of planet development. Atomic and molecular abundances measured from transmission spectroscopy may also probe where the planet originally formed and at what point in its lifetime it moved to its current orbit (Öberg et al. 2011; Dawson & Johnson 2018).

In addition, observations of the strengths of atomic and molecular features will constrain the strength of vertical mixing and resulting amount of chemical disequilibrium in this planet’s atmosphere, and test theories of planet inflation and atmospheric mixing, which are predicted to change for planets below and above 1000 K (Komacek et al. 2019; Baxter et al. 2021). As TOI-4329b likely crossed this threshold in its near past, the level of chemical disequilibrium seen here will be informative regarding the timescales of these mixing processes.

## 8. Orbital Decay of the Evolved Planet Population

The expected tidal interaction between hot gas giant planets and evolved host stars is expected to result in rapid orbital decay and eventual engulfment of the planet. However, orbital decay has only been measured in one system to date, which was significantly less evolved than the systems studied here. By constraining the rate of orbital decay in these systems, we can measure the strength of star–planet tidal interactions and their dependence on star and planet properties.

Based on the TESS and ground-based data currently available for this system, we measure the individual transit times as observed by TESS and LCOGT and fit them using a quadratic model through the `exoplanet` TTVOrbit package. We choose to include only the LCOGT observations from Teide Observatory, as they give more consistent and numerous transit times than can be derived from the McDonald Observatory observations, which were more strongly affected by poor weather conditions. We illustrate our measured transit times and best-fit quadratic model in Figure 13.

Our best-fit model does not significantly prefer orbital decay to describe this system. Most importantly, the transit times measured by LCOGT and the TESS Extended Mission appear to be in strong agreement with the expected transit times for

this system, implying that any orbital decay in this system has not changed the ephemerides of transit by  $>0.02$  day, and thus is not yet measurable. This implies that the change in period of this system is  $<1$  s per year, and following the “constant phase lag” formulation of Goldreich & Soter (1966) used in recent orbital decay detection, this corresponds to  $Q'_* > 2 \times 10^4$ , in agreement with what has been found for other systems where orbital decay has been constrained (Chontos et al. 2019; Patra et al. 2020; Yee et al. 2020). A longer baseline of 2 minutes cadence TESS data for TOI-2337b will provide tighter constraints on the orbital decay rate of this system. Given the more limited data sets available for TOI-4329b and TOI-2669b, we do not attempt to measure orbital decay in these systems.

Figure 14 illustrates the population of known planets, highlighting those planets that are most likely to be experiencing strong orbital decay, as well as decay rates predicted using the equilibrium tide model of Goldreich & Soter (1966). The planets with the smallest relative orbital separations and highest masses relative to their stars decay most quickly, and can be found in the upper left-hand corner of this plot. We have illustrated the new planets found by this survey as squares on this plot. These planets are among some of the best candidates for detecting orbital decay. In particular, TOI-2337b is predicted to be the most rapidly decaying planet known to date. In addition, TOI-2337b also orbits a relatively cool star, which is expected to increase the speed of its orbital decay due to more rapid tidal dissipation in TOI-2337’s thick outer convective envelope (Patra et al. 2020). Additional TESS data from the Extended TESS Mission will be essential to constraining the transit ephemerides and thus the orbital properties and stellar tidal quality factor for this system.

Based on the orbital properties of these systems and theoretical assumptions about binary system evolution (Zahn 1977; Hut 1981; Zahn 1989; Zahn & Bouchet 1989), we can infer the initial orbital properties, relevant energy dissipation rates, and stellar structure constraints that could not be probed in other systems. Figure 15 illustrates the strength of various tides and the expected evolutionary tracks for TOI-2337b and TOI-2337. The tidal quality factor of TOI-2337,  $Q'_*$ , is highly dependent on the evolutionary processes. Assuming a tidal quality factor for this star of  $2 \times 10^5$  as measured in WASP-12b (Yee et al. 2020; Turner et al. 2021), we can predict the orbital decay of TOI-2337b by assuming an



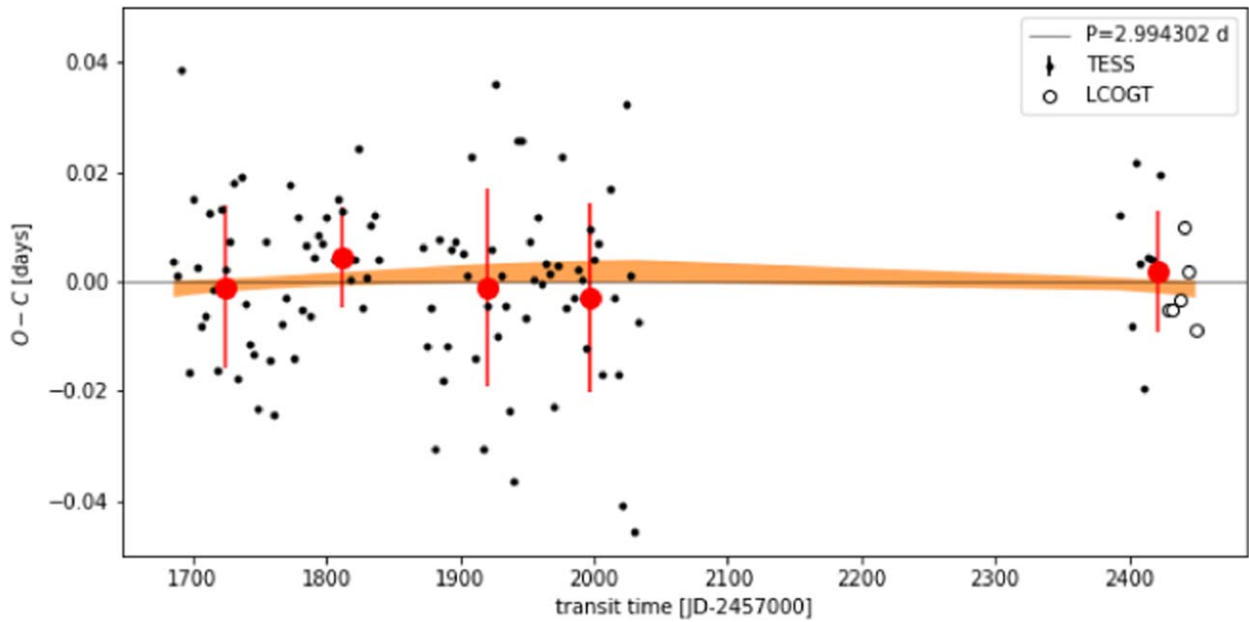


**Figure 13.** Transit times of TOI-2337b from TESS and LCOGT Teide observations as measured by the `exoplanet` TTVOrbit package. We use a quadratic formula to describe the evolution of transit times and do not detect any clear orbital decay in this system. Although there is still a great deal of scatter in the measured transit times from our current data for this system, additional TESS Extended Mission data have only just become available and should constrain the orbital decay rate of this system to a significantly higher precision by the end of next year.

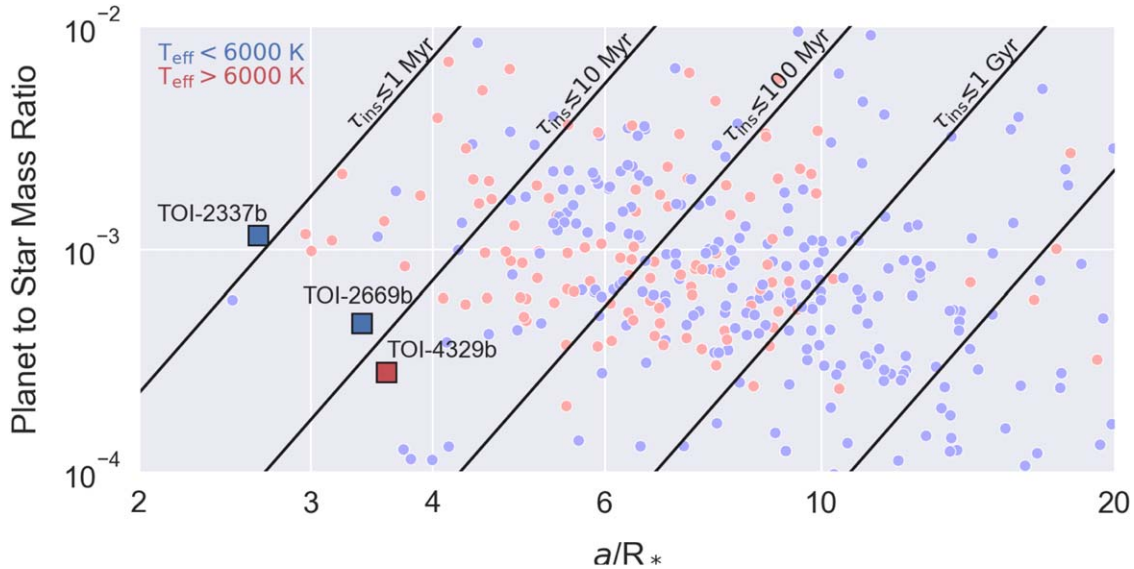


**Figure 14.** Semimajor axis divided by stellar radius vs. planet to star mass ratio for confirmed planets. Orbital decay timescales decrease toward the upper left of this plot, and black diagonals correspond to theorized rates of orbital decay, where the leftmost line corresponds to a decay timescale of  $10^6$  yr and each following line increases by a factor of 10. Blue points have stellar effective temperatures  $<6000$  K as reported by the NASA Exoplanet Archive, while red points represent planets around hotter stars. The planets confirmed by this work are shown as squares with black outlines and are populating relatively sparse regions of parameter space on this plot that correspond to rapid orbital decay. In particular, TOI-2337b may be experiencing the fastest rate of orbital decay of any planet known to date.

initial semimajor axis and predicting the orbital evolution of the system. As the combination of orbital period and stellar surface gravity is the most extreme for TOI-2337b, here we approach the dynamical analysis of the TOI-2337 system via the numerical calculation of the tidal energy dissipation rate over time instead of assuming a constant value for  $Q'_*$ .

To estimate the order of magnitude of the rate of change in the semimajor axis and orbit period, we follow the method used in Weinberg et al. (2017) and Sun et al. (2018) for close circular exoplanet systems. The stellar model is constructed with the Modules for Experiments in Stellar Astrophysics

(MESA; Version 12115; Paxton et al. 2011, 2013, 2015, 2018, 2019). The initial metallicity is  $Z = 0.034$  derived from the observed  $[\text{Fe}/\text{H}]$ , assuming the solar metallicity is  $Z = 0.014$  (Asplund et al. 2009). The detailed model for TOI-2337 has an initial mass of  $1.325 M_\odot$ . Combining the initial metallicity, those initial settings yield the sequence of models of the star that are characterized in the  $\log(g) - T_{\text{eff}}$  plane in the bottom panel of Figure 15.

In the top panel of Figure 15, we show the orbital semimajor axis as a function of  $\log(g)$  using the stellar model described in the last paragraph, where  $\log(g)$  operates as a proxy for the

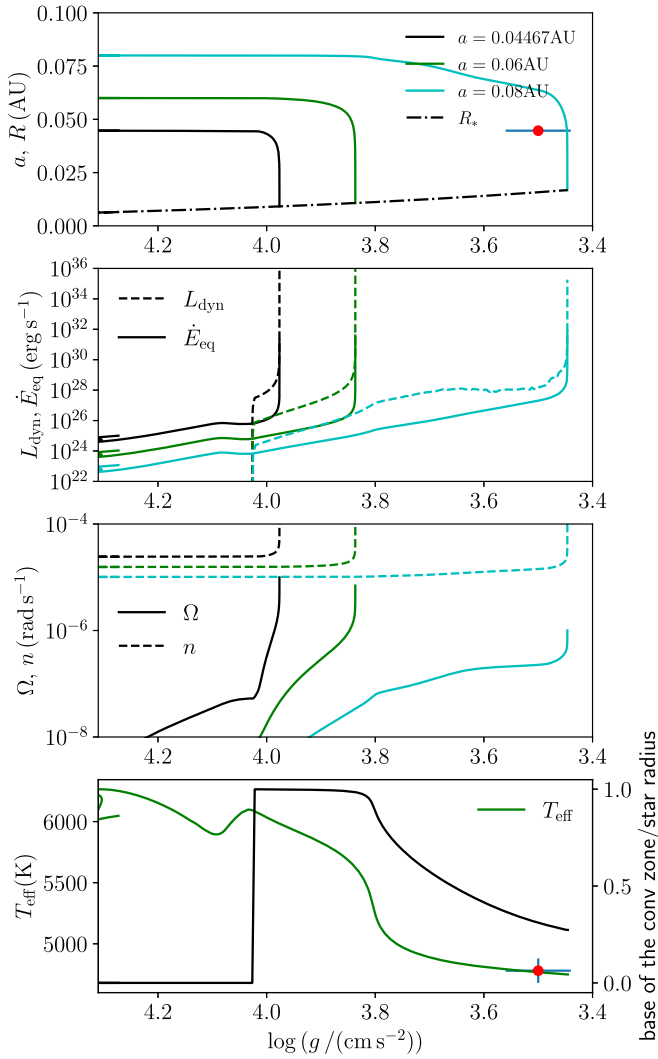


**Figure 15.** Top: semimajor axis vs.  $\log(g)$ , as well as evolutionary models for TOI-2337b. Second panel: energy generated by dynamical and equilibrium tides during the inspiral of TOI-2337b, as a function of  $\log(g)$ . At all evolutionary states, dynamical tides appear to dominate over equilibrium effects. Third panel: rotational frequency vs.  $\log(g)$ , where  $\Omega$  indicates stellar rotation and  $n$  indicates orbital period. The orbital period is significantly shorter than the stellar rotation at all relevant  $\log(g)$  values. Bottom panel: stellar structure and effective temperature as a function of  $\log(g)$ . As the host star TOI-2337 evolves, the convection zone first disappears from the core of the star, then deepens from the surface while the effective temperature decreases.

evolutionary state of the host star. The orbital decay rate is calculated by using Equation (1) in Sun et al. (2018). Colored lines illustrate evolutionary pathways for different initial orbital separations, and the red point illustrates the system as seen today, thus indicating that only the light blue model is consistent with the existence of this system. Note that the black solid line corresponds to an initial semimajor axis of 0.04467 au, which is the current orbital separation of the TOI-2337 system. At this initial orbital separation, the system should merge at  $\log(g) \sim 4$ , significantly higher than the observed  $\log(g) = 3.5$ . This implies TOI-2337b began its life at a larger semimajor axis and is undergoing rapid orbital decay as dynamical tides overwhelm equilibrium tides and runaway planetary inspiral occurs (Sun et al. 2018). The short orbital period and low surface gravity of the TOI-2337b system imply the inspiral process must be ongoing.

Given the uncertainty in the measurement of the stellar mass and metallicity of the TOI-2337 system, and the sensitivity of the evolutionary history of the star to the initial mass and metallicity, we determine a range of the rate of change in semimajor axis and orbital period assuming different initial mass and metallicity. Our numerical simulations predict that dynamical tides should dominate over the effect of equilibrium tides and estimate the orbital decay timescale of the TOI-2337 system to be between 1 and 10 Myr.

The second panel of Figure 15 illustrates the change in tidal energy dissipation as a function of  $\log(g)$ , where solid lines correspond to equilibrium tides (calculated using Equation (5) from Sun et al. 2018), while dashed lines correspond to dynamical tides (Equation (14) from Sun et al. 2018). Once TOI-2337 began evolving off the main sequence, dynamical tides dominated the system, resulting in eventual runaway orbital decay. The exact timing of this runaway orbital decay depends both on the orbital properties of the system as well as the internal structure of the host star (Weinberg et al. 2017).

The third panel of Figure 15 illustrates stellar rotational frequency (solid lines) and orbital frequency (dashed lines) as a function of  $\log(g)$ . To simplify the problem, we assume a zero rotation rate of the star at the zero-age main sequence, but note that this evolution analysis is not sensitive to the initial rotation rate of the star. In the TOI-2337 system, like the WASP-12 system, the planet TOI-2337b should be synchronized. In addition, TOI-2337b does not have enough orbital angular momentum to synchronize the host star, and thus the star’s spin rate is always smaller than the orbital frequency. Most of the tidal dissipation energy is therefore generated in the non-synchronized primary star.

Finally, the bottom panel shows the stellar effective temperature and the location of the base of the stellar convection zone as a function of stellar surface gravity. As TOI-2337 evolves across the subgiant phase, it becomes cooler, its core becomes radiative near  $\log(g) \sim 4$  and its convective envelope grows deeper over time. The tidal dissipation rate is affected by the exact location of this boundary in the star. The location of this boundary is highly variable during the subgiant and early red giant phase of evolution, thus introducing degeneracies between different models of stars on the subgiant branch (Tayar et al. 2020). Future observation of or upper limits on orbital decay in the TOI-2337 and similar systems will better constrain the value of  $Q'_*$ , breaking degeneracies between subgiant stellar models and updating our ability to constrain stellar structure during subgiant and red giant branch stellar evolution.

## 9. Conclusions

We have conducted a search for planets transiting evolved stars using TESS Full Frame Image data. Our search for planets around evolved stars uncovered TOI-2337b, TOI-4329b, and TOI-2669b, two of which are the shortest-period planets orbiting evolved stars ( $R_* > 2 R_\odot$ ,  $T_{\text{eff}} < 6000 \text{ K}$ ) found to date. These planets display a diverse range of properties and offer new glimpses of the final stages of planetary system evolution. Our main conclusions are as follows:

1. TOI-2337b is a massive, uninflated planet ( $1.6 M_J$ ,  $0.9 R_J$ ) on the shortest-period orbit ( $P = 2.9943$  days) ever observed around a red giant ( $3.2 R_\odot$ ,  $1.4 M_\odot$ ) star. Despite its high incident flux, it is not inflated nor on an

eccentric orbit, and appears to be inducing ellipsoidal variations in its host star. Finally, based on estimates of tidal inspiral in evolved systems, the tidal decay of this planet should be measurable by TESS on a timescale of years. Current constraints indicate orbital decay is not yet measurable in this system, and we constrain the modified tidal quality factor of the star  $Q'_* > 2 \times 10^4$ , in agreement with values found in other short-period hot Jupiter systems. Tighter constraints on this value made from  $\geq 1$  yr of observations from the TESS Extended Mission data may constrain the location of the star's radiative–convective boundary, as it is strongly dependent on the properties of wave propagation through the stellar interior.

2. TOI-4329b is a less massive planet ( $0.5 M_J$ ) on an even shorter orbit ( $P = 2.923$  days) around a subgiant host ( $2.3 R_\odot$ ,  $1.5 M_\odot$ ). In contrast to TOI-2337b, TOI-4329b is highly inflated ( $1.5 R_J$ ), and there are no signs of out-of-transit phase variations in the system. Its orbit appears circular. Its high level of inflation and short period make it suitable for atmospheric observation. Transmission spectroscopy of these (and similar) planets will be valuable to test the validity of planet reinflation and evolution metrics.
3. TOI-2669b is the most evolved system in our sample, on the longest-period orbit ( $1.7 R_J$ ,  $0.7 M_J$  planet orbiting a  $4.2 R_\odot$ ,  $1.3 M_\odot$  star every 6.2 days). Though the data for this sample are still limited, the brightness of this target also make it potentially amenable for transmission spectroscopy with JWST. In addition, tighter constraint on the eccentricity ( $e < 0.15$ ) observed in the system could place new constraints on planet inflation and migration mechanisms and timescales.
4. These planets display a wide range of inflation efficiencies. When considered with the previously known population of evolved inflated planets, the evolved planet population appears to be relatively underinflated for a given incident flux, regardless of planet mass. This indicates that a mass–radius–flux relation may not be sufficient to describe the entire inflated planet population.

Detailed stellar spectral analysis can reveal evidence for elements that are short-lived at the surfaces in giant stars, such as lithium and refractory elements. Detection of large amounts of lithium in addition to refractory elements with high condensation temperatures such as magnesium, aluminum, calcium, and silicon in giant stars is thus an indication of recent planet engulfment (Oh et al. 2018; Soares-Furtado et al. 2021). A more detailed analysis of previously acquired Keck HIRES spectra of these stars can reveal the relative enhancement of the above elements in these systems.

TESS Extended Mission operations will be essential for improving planet parameters as well as stellar parameters for these systems. This has already been shown to be the case for TOI-2669b, where TESS Extended Mission data both improved the period precision by an order of magnitude and also revealed potential asteroseismic signals of the star. We expect that the higher cadence and longer baseline Extended Mission observations of TOI-2337b and TOI-4329b may allow asteroseismic characterization of these stars as well.

The additional signal and higher cadence available for TESS Extended Mission observations will also improve our ability to measure transit parameters, as well as any other out-of-transit

phase variability. Such variability has been measured for several main-sequence systems with higher cadence data from the TESS nominal mission (Wong et al. 2020, 2021).

It has been observed that hot Jupiters orbiting stars cooler than 6250 K tend to have low obliquities (Winn et al. 2010). Several hypotheses have been introduced to explain this, such as the damping of inclination by the stellar convective envelope (Winn et al. 2010) or magnetic realignment of stellar orbits during pre-main-sequence evolution (Spalding & Batygin 2015). Given that the systems studied here have evolved from hot stars with thin convective envelopes on the main sequence to giants with thick convective envelopes, measuring the obliquity of these newly confirmed planets can distinguish between these theorized mechanisms for spin–orbit alignment in hot Jupiter systems. Measuring the Rossiter–McLaughlin (RM) effect (McLaughlin 1924; Rossiter 1924) for these systems with extreme precision radial velocity instruments could reveal trends of planetary system obliquities with respect to stellar mass (Cabot et al. 2021; Rubenzahl et al. 2021) and constrain models of hot Jupiter formation (e.g., Dawson & Johnson 2018; Albrecht et al. 2021). Stellar obliquity can also be constrained via asteroseismology (Huber et al. 2013) and thus future asteroseismic detections for these systems, in combination with future RM measurements, could reveal true system obliquities.

Transmission spectroscopy of exoplanet atmospheres has been carried out successfully from ground-based facilities (Hoeijmakers et al. 2020; Giacobbe et al. 2021). These observations allowed identification of atmospheric metals and/or molecular species that provide insight into the formation conditions for these planets through elemental and refractory/volatile ratios (Lothringer et al. 2021). Observation of emission features before and during planet occultations from ground-based facilities may prove more promising. Indications of atmospheric outflows, first observed using the Hubble Space Telescope (Spake et al. 2018), have now been accomplished from ground-based narrowband photometry (Vissapragada et al. 2020; Paragas et al. 2021). The more extreme environments of these planets warrant a search for atmospheric outflows, which should be occurring at a faster rate and thus may be observable from ground-based facilities. Otherwise, upcoming space-based observatories such as the JWST will likely be required to probe the atmospheric signal of these planets.

Detailed kinematic information for these stars allow investigation into differences between known moving groups and distinct kinematic groups throughout the Milky Way. Given the intrinsic brightness of evolved stars, among magnitude-limited surveys for planets such as TESS, evolved systems will be the first to reveal planetary demographics outside of the thin disk of our Galaxy.











We thank Howard Isaacson and Daniel Foreman-Mackey for helpful discussions. We acknowledge the use of public TESS data from pipelines at the TESS Science Office and at the TESS Science Processing Operations Center. Resources supporting this work were provided by the NASA High-End Computing (HEC) Program through the NASA Advanced Supercomputing (NAS) Division at Ames Research Center for the production of the SPOC data products. This work was supported by a NASA Keck PI Data Award, administered by the NASA Exoplanet Science Institute. Data presented herein were obtained at the W. M. Keck Observatory from telescope time allocated to the




National Aeronautics and Space Administration through the agency's scientific partnership with the California Institute of Technology and the University of California. The Observatory was made possible by the generous financial support of the W. M. Keck Foundation. The authors wish to recognize and acknowledge the very significant cultural role and reverence that the summit of Maunakea has always had within the indigenous Hawaiian community. We are most fortunate to have the opportunity to conduct observations from this mountain. S.G., N.S., and D.H. acknowledge support by the National Aeronautics and Space Administration under grant 80NSSC19K0593 issued through the TESS Guest Investigator Program. D.H. acknowledges support from the Alfred P. Sloan Foundation and the National Aeronautics and Space Administration (80NSSC21K0652), and the National Science Foundation (80NSSC21K0652). N.S., A.C., and M.R. acknowledge support from the National Science Foundation through the Graduate Research Fellowship Program under grants 1842402 and DGE-1752134. Any opinions, findings, and conclusions or recommendations expressed in this material are those of the authors and do not necessarily reflect the views of the National Science Foundation. M.S. acknowledges funding support from NSF ACI-1663696 and AST-1716436. T.D.K. acknowledges support from the 51 Pegasi b fellowship in Planetary Astronomy sponsored by the Heising-Simons Foundation. P.D. is supported by a National Science Foundation (NSF) Astronomy and Astrophysics Postdoctoral Fellowship under award AST-1903811. This research has made use of the Exoplanet Follow-up Observation Program website, which is operated by the California Institute of Technology, under contract with the National Aeronautics and Space Administration under the Exoplanet Exploration Program. Funding for the TESS mission is provided by NASA's Science Mission Directorate.

*Software:* This work relied heavily on open source software tools, and we would like to thank the developers for their contributions to the astronomy community. For data access and detrending, this research made use of *lightkurve*, a Python package for Kepler and TESS data analysis (Lightkurve Collaboration et al. 2018), *TESSCut*, a MAST tool for extracting observations from TESS FFIs (Brasseur et al. 2019), and *eleanor*, a pipeline for producing and detrending TESS FFI light curves (Feinstein et al. 2019). The analysis portion of this research relied on *astropy* (Astropy Collaboration et al. 2013, astropy2018), as well as *exoplanet* (Foreman-Mackey et al. 2020) and its dependencies (Agol et al. 2020; Foreman-Mackey et al. 2020; Kipping 2013; Luger et al. 2019; Salvatier et al. 2016; Theano Development Team 2016).

### ORCID iDs

Samuel K. Grunblatt  <https://orcid.org/0000-0003-4976-9980>  
 Nicholas Saunders  <https://orcid.org/0000-0003-2657-3889>  
 Meng Sun  <https://orcid.org/0000-0001-9037-6180>  
 Ashley Chontos  <https://orcid.org/0000-0003-1125-2564>  
 Melinda Soares-Furtado  <https://orcid.org/0000-0001-7493-7419>  
 Nora Eisner  <https://orcid.org/0000-0002-9138-9028>  
 Filipe Pereira  <https://orcid.org/0000-0002-2157-7146>  
 Thaddeus Komacek  <https://orcid.org/0000-0002-9258-5311>  
 Daniel Huber  <https://orcid.org/0000-0001-8832-4488>  
 Karen Collins  <https://orcid.org/0000-0001-6588-9574>

Gavin Wang  <https://orcid.org/0000-0003-3092-4418>  
 Chris Stockdale  <https://orcid.org/0000-0003-2163-1437>  
 Samuel N. Quinn  <https://orcid.org/0000-0002-8964-8377>  
 Rene Tronsgaard  <https://orcid.org/0000-0003-1001-0707>  
 George Zhou  <https://orcid.org/0000-0002-4891-3517>  
 Grzegorz Nowak  <https://orcid.org/0000-0002-7031-7754>  
 Hans J. Deeg  <https://orcid.org/0000-0003-0047-4241>  
 David R. Ciardi  <https://orcid.org/0000-0002-5741-3047>  
 Andrew Boyle  <https://orcid.org/0000-0001-6037-2971>  
 Malena Rice  <https://orcid.org/0000-0002-7670-670X>  
 Fei Dai  <https://orcid.org/0000-0002-8958-0683>  
 Sarah Blunt  <https://orcid.org/0000-0002-3199-2888>  
 Judah Van Zandt  <https://orcid.org/0000-0002-4290-6826>  
 Corey Beard  <https://orcid.org/0000-0001-7708-2364>  
 Joseph M. Akana Murphy  <https://orcid.org/0000-0001-8898-8284>  
 Paul A. Dalba  <https://orcid.org/0000-0002-4297-5506>  
 Jack Lubin  <https://orcid.org/0000-0001-8342-7736>  
 Casey Lynn Brinkman  <https://orcid.org/0000-0002-4480-310X>  
 Andrew W. Howard  <https://orcid.org/0000-0001-8638-0320>  
 Lars A. Buchhave  <https://orcid.org/0000-0003-1605-5666>  
 Ruth Angus  <https://orcid.org/0000-0003-4540-5661>  
 George R. Ricker  <https://orcid.org/0000-0003-2058-6662>  
 Jon M. Jenkins  <https://orcid.org/0000-0002-4715-9460>  
 Bill Wohler  <https://orcid.org/0000-0002-5402-9613>  
 Robert F. Goeke  <https://orcid.org/0000-0003-1748-5975>  
 Alan M. Levine  <https://orcid.org/0000-0001-8172-0453>  
 Knicole D. Colon  <https://orcid.org/0000-0001-8020-7121>  
 Chelsea X. Huang  <https://orcid.org/0000-0003-0918-7484>  
 Michelle Kunitomo  <https://orcid.org/0000-0001-9269-8060>  
 Avi Shporer  <https://orcid.org/0000-0002-1836-3120>  
 David W. Latham  <https://orcid.org/0000-0001-9911-7388>  
 Sara Seager  <https://orcid.org/0000-0002-6892-6948>  
 Roland K. Vanderspek  <https://orcid.org/0000-0001-6763-6562>  
 Joshua N. Winn  <https://orcid.org/0000-0002-4265-047X>

### References

- Agol, E., Luger, R., & Foreman-Mackey, D. 2020, *AJ*, 159, 123  
 Aguirre, V. S., Stello, D., Stokholm, A., et al. 2020, *ApJL*, 889, L34  
 Albrecht, S. H., Marcussen, M. L., Winn, J. N., Dawson, R. I., & Knudstrup, E. 2021, *ApJL*, 916, L1  
 Almenara, J. M., Damiani, C., Bouchy, F., et al. 2015, *A&A*, 575, A71  
 Asplund, M., Grevesse, N., Sauval, A. J., & Scott, P. 2009, *ARA&A*, 47, 481  
 Astropy Collaboration, Robitaille, T. P., Tollerud, E. J., et al. 2013, *A&A*, 558, A33  
 Barclay, T., Endl, M., Huber, D., et al. 2015, *ApJ*, 800, 46  
 Barclay, T., Pepper, J., & Quintana, E. V. 2018, *ApJS*, 239, 2  
 Batalha, N. E., Mandell, A., Pontoppidan, K., et al. 2017, *PASP*, 129, 064501  
 Baxter, C., Désert, J.-M., Tsai, S.-M., et al. 2021, *A&A*, 648, A127  
 Bell, T. J., Zhang, M., Cubillos, P. E., et al. 2019, *MNRAS*, 489, 1995  
 Benneke, B. 2015, arXiv:1504.07655  
 Brasseur, C. E., Phillip, C., Fleming, S. W., Mullally, S. E., & White, R. L. 2019, Astrocut: Tools for creating cutouts of TESS images, ascl:1905.007  
 Cabot, S. H. C., Bello-Arufe, A., Mendonça, J. M., et al. 2021, *AJ*, 162, 218  
 Carlberg, J. K., Cunha, K., Smith, V. V., & Majewski, S. R. 2013, *AN*, 334, 120  
 Choi, J., Dotter, A., Conroy, C., et al. 2016, *ApJ*, 823, 102  
 Chontos, A., Huber, D., Sayeed, M., & Yamsiri, P. 2021, arXiv:2108.00582  
 Chontos, A., Huber, D., Latham, D. W., et al. 2019, *AJ*, 157, 192  
 Collins, K. A., Kielkopf, J. F., Stassun, K. G., & Hessman, F. V. 2017, *AJ*, 153, 77  
 Dawson, R. I., & Johnson, J. A. 2018, *ARA&A*, 56, 175  
 Demory, B.-O., & Seager, S. 2011, *ApJS*, 197, 12  
 Dotter, A. 2016, *ApJS*, 222, 8

- Eisner, N. L., Barragán, O., Aigrain, S., et al. 2020, *MNRAS*, 494, 750
- Faigler, S., & Mazeh, T. 2011, *MNRAS*, 415, 3921
- Feinstein, A. D., Montet, B. T., Foreman-Mackey, D., et al. 2019, *PASP*, 131, 094502
- Foreman-Mackey, D., Luger, R., Czekala, I., et al. 2020, exoplanet-dev/exoplanet v0.3.2, Zenodo, doi:10.5281/zenodo.1998447
- Gaia Collaboration, Brown, A. G. A., Vallenari, A., et al. 2018, *A&A*, 616, A1
- Giacobbe, P., Brogi, M., Gandhi, S., et al. 2021, *Natur*, 592, 205
- Goldreich, P., & Soter, S. 1966, *Icar*, 5, 375
- Grunblatt, S. K., Huber, D., Gaidos, E., et al. 2019, *AJ*, 158, 227
- Grunblatt, S. K., Huber, D., Gaidos, E. J., et al. 2016, *AJ*, 152, 185
- Grunblatt, S. K., Huber, D., Gaidos, E., et al. 2017, *AJ*, 154, 254
- Grunblatt, S. K., Huber, D., Gaidos, E., et al. 2018, *ApJL*, 861, L5
- Grunblatt, S. K., Zinn, J. C., Price-Whelan, A. M., et al. 2021, *ApJ*, 916, 88
- Guerrero, N. M., Seager, S., Huang, C. X., et al. 2021, *ApJS*, 254, 39
- Hatzes, A. P., Cochran, W. D., Endl, M., et al. 2003, *ApJ*, 599, 1383
- Hoeijmakers, H. J., Seidel, J. V., Pino, L., et al. 2020, *A&A*, 641, A123
- Hon, M., Huber, D., Kuzslewicz, J. S., et al. 2021, *ApJ*, 919, 131
- Howard, A. W., Marcy, G. W., Bryson, S. T., et al. 2012, *ApJS*, 201, 15
- Huber, D., Stello, D., Bedding, T. R., et al. 2009, *CoAst*, 160, 74
- Huber, D., Chaplin, W. J., Christensen-Dalsgaard, J., et al. 2013, *ApJ*, 767, 127
- Huber, D., Zinn, J., Bojsen-Hansen, M., et al. 2017, *ApJ*, 844, 102
- Huber, D., Chaplin, W. J., Chontos, A., et al. 2019, *AJ*, 157, 245
- Hut, P. 1981, *A&A*, 99, 126
- Jenkins, J. M., Twicken, J. D., McCauliff, S., et al. 2016, *Proc. SPIE*, 9913, 99133E
- Jensen, E. 2013, Tapir: A web interface for transit/eclipse observability, Astrophysics Source Code Library, ascl:1306.007
- Kempton, E. M. R., Bean, J. L., Louie, D. R., et al. 2018, *PASP*, 130, 114401
- Kipping, D. M. 2013, *MNRAS*, 435, 2152
- Kipping, D. M. 2013, *MNRAS*, 434, L51
- Kipping, D. M. 2013, *MNRAS*, 435, 2152
- Kjeldsen, H., & Bedding, T. R. 1995, *A&A*, 293, 87
- Komacek, T. D., Showman, A. P., & Parmentier, V. 2019, *ApJ*, 881, 152
- Komacek, T. D., Thorngren, D. P., Lopez, E. D., & Ginzburg, S. 2020, *ApJ*, 893, 36
- Lightkurve Collaboration, Cardoso, J. V. d. M., Hedges, C., et al. 2018, Lightkurve: Kepler and TESS time series analysis in Python, Astrophysics Source Code Library, ascl:1812.013
- Lillo-Box, J., Barrado, D., Moya, A., et al. 2014, *A&A*, 562, A109
- Line, M. R., Knutson, H., Wolf, A. S., & Yung, Y. L. 2014, *ApJ*, 783, 70
- Lopez, E. D., & Fortney, J. J. 2016, *ApJ*, 818, 4
- Lothringer, J. D., Rustamkulov, Z., Sing, D. K., et al. 2021, *ApJ*, 914, 12
- Luger, R., Agol, E., Foreman-Mackey, D., et al. 2019, *AJ*, 157, 64
- Luger, R., Kruse, E., Foreman-Mackey, D., Agol, E., & Saunders, N. 2018, *AJ*, 156, 99
- Mackereth, J. T., Miglio, A., Elsworth, Y., et al. 2021, *MNRAS*, 502, 1947
- MacLeod, M., Cantiello, M., & Soares-Furtado, M. 2018, *ApJL*, 853, L1
- McCully, C., Volgenau, N. H., Harbeck, D.-R., et al. 2018, *Proc. SPIE*, 10707, 107070K
- McLaughlin, D. B. 1924, *ApJ*, 60, 22
- Nielsen, L. D., Bouchy, F., Turner, O., et al. 2019, *A&A*, 623, A100
- Öberg, K. I., Murray-Clay, R., & Bergin, E. A. 2011, *ApJL*, 743, L16
- Oh, S., Price-Whelan, A. M., Brewer, J. M., et al. 2018, *ApJ*, 854, 138
- Paragas, K., Vissapragada, S., Knutson, H. A., et al. 2021, *ApJL*, 909, L10
- Paredes, L. A., Henry, T. J., Quinn, S. N., et al. 2021, *AJ*, 162, 176
- Patra, K. C., Winn, J. N., Holman, M. J., et al. 2020, *AJ*, 159, 150
- Paxton, B., Bildsten, L., Dotter, A., et al. 2011, *ApJS*, 192, 3
- Paxton, B., Cantiello, M., Arras, P., et al. 2013, *ApJS*, 208, 4
- Paxton, B., Marchant, P., Schwab, J., et al. 2015, *ApJS*, 220, 15
- Paxton, B., Schwab, J., Bauer, E. B., et al. 2018, *ApJS*, 234, 34
- Paxton, B., Smolec, R., Schwab, J., et al. 2019, *ApJS*, 243, 10
- Petigura, E. A. 2015, PhD thesis, University of California, Berkeley
- Price-Whelan, A. M., Sipőcz, B. M., Günther, H. M., et al. 2018, *AJ*, 156, 123
- Rappaport, S., Sanchis-Ojeda, R., Rogers, L. A., Levine, A., & Winn, J. N. 2013, *ApJL*, 773, L15
- Ricker, G. R., Winn, J. N., Vanderspek, R., et al. 2014, *JATIS*, 1, 1
- Rossiter, R. A. 1924, *ApJ*, 60, 15
- Rubenzahl, R. A., Dai, F., Howard, A. W., et al. 2021, *AJ*, 161, 119
- Salvatier, J., Wiecki, T. V., & Fonnesbeck, C. 2016, *PeerJ Comp. Sci.*, 2, e55
- Sarkis, P., Mordasini, C., Henning, T., Marleau, G. D., & Mollière, P. 2021, *A&A*, 645, A79
- Saunders, N. K., Grunblatt, S. K., Huber, D., et al. 2022, *AJ*, 163, 53
- Schlaufman, K. C., & Winn, J. N. 2013, *ApJ*, 772, 143
- Sestovic, M., Demory, B.-O., & Queloz, D. 2018, *A&A*, 616, A76
- Shporer, A. 2017, *PASP*, 129, 072001
- Soares-Furtado, M., Cantiello, M., MacLeod, M., & Ness, M. K. 2021, *AJ*, 162, 273
- Spake, J. J., Sing, D. K., Evans, T. M., et al. 2018, *Natur*, 557, 68
- Spalding, C., & Batygin, K. 2015, *ApJ*, 811, 82
- Stassun, K. G., Oelkers, R. J., Paegert, M., et al. 2019, *AJ*, 158, 138
- Sullivan, P. W., Winn, J. N., Berta-Thompson, Z. K., et al. 2015, *ApJ*, 809, 77
- Sun, M., Arras, P., Weinberg, N. N., Troup, N. W., & Majewski, S. R. 2018, *MNRAS*, 481, 4077
- Swain, M. R., Estrela, R., Roudier, G. M., et al. 2021, *AJ*, 161, 213
- Tayar, J., Claytor, Z. R., Huber, D., & van Saders, J. 2020, arXiv:2012.07957
- Teltng, J. H., Avila, G., Buchhave, L., et al. 2014, *AN*, 335, 41
- Theano Development Team 2016, arXiv:1605.02688
- Thorngren, D. P., & Fortney, J. J. 2018, *AJ*, 155, 214
- Thorngren, D. P., Fortney, J. J., Lopez, E. D., Berger, T. A., & Huber, D. 2021, *ApJL*, 909, L16
- Tokovinin, A., Fischer, D. A., Bonati, M., et al. 2013, *PASP*, 125, 1336
- Turner, J. D., Ridden-Harper, A., & Jayawardhana, R. 2021, *AJ*, 161, 72
- Van Eylen, V., Albrecht, S., Gandolfi, D., et al. 2016, arXiv:1605.09180
- Van Eylen, V., Albrecht, S., Huang, X., et al. 2019, *AJ*, 157, 61
- Villaver, E., & Livio, M. 2009, *ApJL*, 705, L81
- Villaver, E., Livio, M., Mustill, A. J., & Siess, L. 2014, *ApJ*, 794, 3
- Vissapragada, S., Knutson, H. A., Jovanovic, N., et al. 2020, *AJ*, 159, 278
- Vogt, S. S., Allen, S. L., Bigelow, B. C., et al. 1994, *Proc. SPIE*, 2198, 362
- Wang, S., Jones, M., Shporer, A., et al. 2019, *AJ*, 157, 51
- Weinberg, N. N., Sun, M., Arras, P., & Essick, R. 2017, *ApJL*, 849, L11
- Weiss, L. M., Marcy, G. W., Rowe, J. F., et al. 2013, *ApJ*, 768, 14
- Welbanks, L., Madhusudhan, N., Allard, N. F., et al. 2019, *ApJL*, 887, L20
- Winn, J. N., Fabrycky, D., Albrecht, S., & Johnson, J. A. 2010, *ApJL*, 718, L145
- Wong, I., Shporer, A., Daylan, T., et al. 2020, *AJ*, 160, 155
- Wong, I., Kitzmann, D., Shporer, A., et al. 2021, *AJ*, 162, 127
- Yee, S. W., Winn, J. N., Knutson, H. A., et al. 2020, *ApJL*, 888, L5
- Zahn, J. P. 1977, *A&A*, 500, 121
- Zahn, J. P. 1989, *A&A*, 220, 112
- Zahn, J. P., & Bouchet, L. 1989, *A&A*, 223, 112
- Zhou, G., Winn, J. N., Newton, E. R., et al. 2020, *ApJL*, 892, L21